Coastal Engineering 191 (2024) 104519

Contents lists available at ScienceDirect

Coastal Engineering

journal homepage: www.elsevier.com/locate/coastaleng

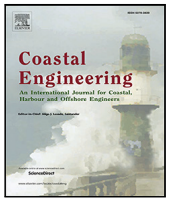

Effects of free surface modelling and wave-breaking turbulence on depth-resolved modelling of sediment transport in the swash zone

J.W.M. Kranenborg [a,*], G.H.P. Campmans [a], J.J. van der Werf [a,b], R.T. McCall [b], A.J.H.M. Reniers [c], S.J.M.H. Hulscher [a]

[a] University of Twente, Enschede, The Netherlands
[b] Deltares, Delft, The Netherlands
[c] Delft University of Technology, Delft, The Netherlands

ARTICLE INFO

Keywords:
Swash zone
Morphodynamics
OpenFOAM
RANS
Sand transport
Numerical modelling

ABSTRACT

The swash zone is an important region for the coastal morphodynamics. Often, model studies of the swash zone use depth-averaged models. These models typically assume a vertically uniform velocity and sand concentration for calculating the sand transport flux. However, this assumption is not always accurate in the swash zone. In order to investigate the vertical distribution of velocity and sand, we use a depth-resolving model that is able to capture these vertical variations. We simulate the flow and suspended sediment transport induced by bichromatic waves using a 2DV depth-resolving RANS model. Our verification of the model shows that special care needs to be taken to deal with bubbles in 2DV simulations. Furthermore, we show that turning off the (Wilcox, 2006, 2008) limiter for turbulence, increases the modelled turbulent kinetic energy that is induced by wave-breaking, resulting in improved predictions of sediment concentrations. Using the depth-resolving model, we show that the vertical distribution of velocity and sand is far from uniform in the swash zone. The results show that if one assumes vertically uniform depth-averaged velocities and concentrations, one can overpredict the sediment flux by 50%.

1. Introduction

The morphodynamics of the coast is largely controlled by the effects of waves and currents on the beach. An important region influencing the coastal morphodynamics is the swash zone. Here, waves intermittently cover and expose the beach face. The swash zone is characterised by strong shallow flows, breaking waves, large amounts of turbulence and the presence of air bubbles (Masselink and Puleo, 2006). These dynamics can lead to large sediment transport fluxes and strong intraswash bed level changes in the order of centimetres per seconds (Blenkinsopp et al., 2011; Van der Zanden et al., 2019a), which make it difficult to study important morphological processes experimentally. Numerical models can provide a valuable tool to complement such experiments for understanding and ultimately predicting the dynamics of the swash zone.

There are different model techniques for understanding intraswash morphodynamics (Briganti et al., 2016). In this paper we distinguish two types of models: depth-averaged and depth-resolving models. In depth-averaged models, the model equations define relations between depth-averaged flow quantities that do not include information of the vertical distribution of the flow quantities. As such, depth-averaged models are relatively computational efficient due to their lower dimensionality. These models can give insight into important processes that drive morphodynamics (see e.g. Reniers et al., 2013; Incelli et al., 2016; Zhu and Dodd, 2020). However, depth-averaged models have difficulty accurately predicting intraswash sediment dynamics, in particular suspended sediment transport (Ruffini et al., 2020; Mancini et al., 2021). Depth-resolving models have shown promising results in terms of their hydrodynamic and morphodynamic predictions (e.g. Li et al., 2019; Kranenborg et al., 2022; García-Maribona et al., 2021). For depth-resolving models, the model equations also describe the variation of flow quantities in the vertical direction. This means that these models resolve important vertical variations in the flow, however, this comes at a cost in computational resources. For this reason, we employ the depth-resolving model technique for gaining insight into important depth-dependent processes, which can be used to improve depth-averaged models.

An important process for the suspended sediment transport is turbulence (Fredsøe and Deigaard, 1992). For instance, Sumer et al. (2013) showed experimentally that eddies created during the wave-breaking process can lead to strong sediment suspension. Some depth-averaged

* Correspondence to: Deltares, Delft, The Netherlands.
E-mail address: joost.kranenborg@deltares.nl (J.W.M. Kranenborg).

https://doi.org/10.1016/j.coastaleng.2024.104519
Received 6 October 2023; Received in revised form 29 March 2024; Accepted 7 April 2024
Available online 8 April 2024

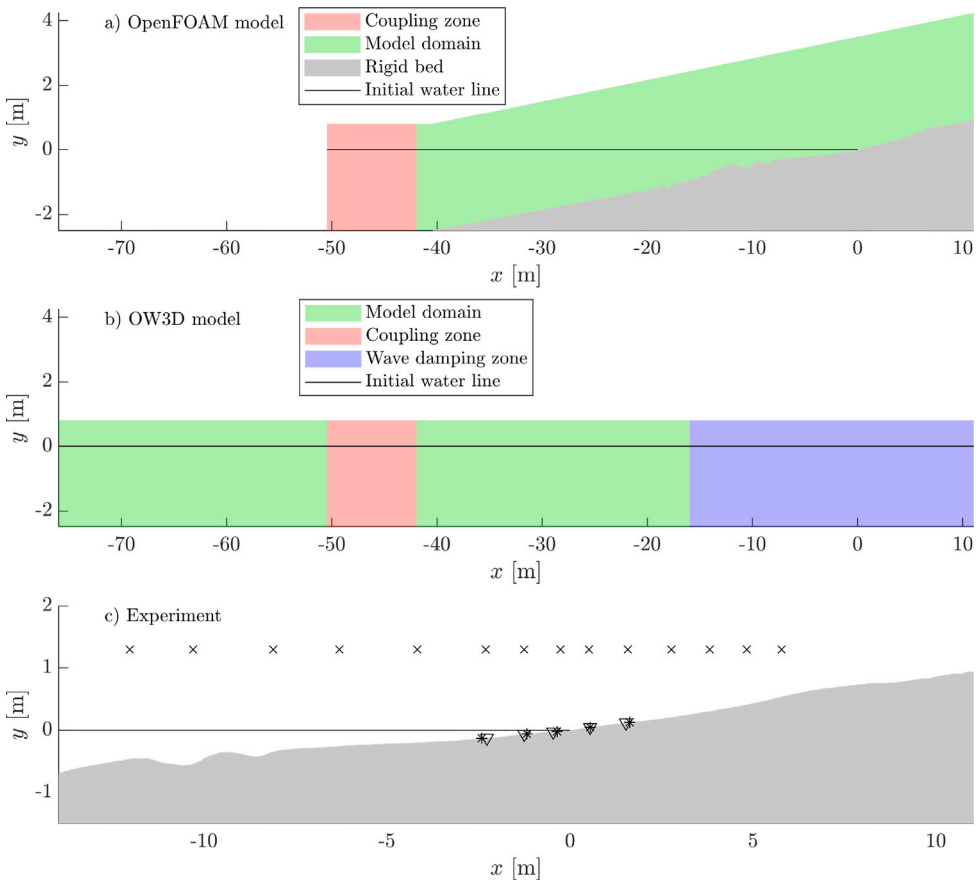

Fig. 1. Schematic showing (a) the depth-resolving model domain and (b) the OW3D model domain. The red region in panels (a) and (b) shows where the one-way coupling from OW3D to OpenFOAM is done. Panel (c) shows the area around the still water line and the probes used in the paper. Here crosses show positions of wave gauges, triangles show ADV probes and stars show OBS probes.

model studies on turbulence and sediment interaction also exist. For instance, Alsina et al. (2009) used a modified version of the model by Deigaard et al. (1986) to model turbulence and found that the contribution of bore-generated turbulence essential to achieve accurate cross-shore suspended sediment transport. Zhu and Dodd (2020) used a different approach by estimating the turbulent kinetic energy from data instead. They found that bore-generated turbulence dominated the sediment entrainment, and is more important than entrainment from pure shear.

A different turbulence-related process is the vertical distribution of suspended sediment and the vertical velocity profile. For instance, (Aagaard et al., 2021) discuss the influence of turbulence on the vertical distribution of sediment in the surf zone. In the swash zone, the study of Sumer et al. (2013) shows that turbulent eddies can rapidly entrain sediment high into the water column, putting clouds of sediment above regions with lower sediment concentration. This was also seen in the model results of Kranenborg et al. (2022), especially in the presence of a backwash bore. The recent depth-averaged study of Mancini et al. (2021) argued that, at least in-part, the difficulty in modelling suspended transport is due to uncertainties in the vertical structure of sediment transport.

Many depth-averaged models incorporate parametrisations to deal with these vertical nonuniformities. For instance, Mancini et al. (2021) uses a bottom boundary layer model, based on a friction coefficient, to account for the vertical profile of the cross-shore velocity. Similarly, for calculating the sediment deposition, they use a power-law profile (Soulsby, 1997) to calculate the near-bed sediment concentration. The method of Galappatti and Vreugdenhil (1985), which is used by for example Reniers et al. (2013), uses a different concept to account for the flow conditions, namely the introduction of an equilibrium sediment concentration and an adaptation time. These examples all use information about the vertical distribution. However, this information is only applied to calculations of erosion and deposition fluxes, and not for the cross-shore flux of sediment. The importance of vertical structures in the cross-shore sediment flux is not well understood.

To investigate the importance of vertical structures, we employ a depth-resolving model. There are different approaches for both the flow and sediment modelling in a depth-resolving way. In this study we limit ourselves to using the Reynolds Averaged Navier Stokes (RANS) approach, combined with modelling suspended sediment as a passive scalar that is transported and diffused with the flow. Such models have been used previously to analyse breaker bar morphodynamics (Jacobsen and Fredsoe, 2014a,b) and swash-zone morphodynamics induced by solitary waves (Li et al., 2019; Kranenborg et al., 2022). These studies all use models that are based on the original model by Jacobsen et al. (2014), implemented in the OpenFOAM framework. The (Jacobsen et al., 2014) model uses the Volume of Fluid (VoF) method to discriminate between air and water in the solution. Recently, a different model based on the IH2VOF model was used to study morphodynamics and intraswash suspended sediment dynamics under bichromatic waves (García-Maribona et al., 2021, 2022). An important difference between the IH2VOF studies and the studies by Li et al. (2019) and Kranenborg et al. (2022), is that they use different implementations of the VoF method. Where typical VoF implementations compute the RANS equations in both the air and water phases, the IH2VOF model instead compute the RANS equations in the water phase only.

The presence of an air phase in the VoF method means that care needs to taken around the air/water interface. For instance, unphysical layers of air can remain sticking close to a body in a phenomenon called

numerical ventilation, leading to an incorrect decrease of skin friction (Gray-Stephens et al., 2019). Furthermore, the modelled behaviour of air bubbles is related to the 2DV approach typically employed in depth-resolved swash zone studies, which disregards 3D effects.

In this paper, we investigate the importance of wave-breaking turbulence and vertical nonuniformities for sediment transport in the swash zone. To this end we use the model by Kranenborg et al. (2022). First, we will investigate the effects of air entrainment and bubbles in the model on the swash flow. Furthermore, the effects of the turbulence limiter introduced by Wilcox (2006, 2008) are investigated. Finally, we use the depth-resolved model to determine nonuniform vertical structures in suspended sediment concentration and flow velocity, and how they influence the calculated suspended sediment flux. To study these processes we formulate the following research questions for this paper:

- What is the effect of the air entrainment and bubbles in a 2DV VoF model and how does it influence sediment transport?
- What is the influence of the (Wilcox, 2006) limiter on wave-breaking turbulence and sediment transport?
- How does the vertical distribution of sediment concentration and flow velocity influence the sediment transport flux?

In Section 2, the research methodology is described. Section 3 presents the model verification and the role of bubbles and wave-breaking turbulence. Section 4 presents model results on the importance of vertical structures in the suspended sediment transport flux. The results are subsequently discussed in Section 5 and the research questions are answered in 6.

2. Methodology

We start by describing the experimental conditions used as a basis for the analysis. Subsequently, the model and its implementation, domain and initial and boundary conditions are described. Finally, the definitions of metrics and analysis tools are laid out.

2.1. Experiment description

To investigate sediment transport and vertical structures therein, we need an experiment that includes the relevant processes. Solitary waves are too simple for this purpose as they do not produce wave-swash interactions, or the advection of pre-suspended sediment. These are both processes which are often thought to be important (Van der Zanden et al., 2019b). Furthermore, we need detailed time-series of suspended sediment concentrations and velocities to verify the model performance. For these reasons, we opt to use the bichromatic wave experiments by Van der Zanden et al. (2019a). This enables both an analysis of suspended sediment which includes processes mentioned above, and makes it possible to make averages over wave group repetitions.

Van der Zanden et al. (2019a) divided up their experiments in smaller wave runs to measure the evolution of the profile over time. We use the initial morphology from run no 5 which starts at 180 min after the first wave run (see Fig. 1 for the initial profile of run 5). The experiments were conducted in the large-scale CIEM wave flume at the Universitat Politécnica de Catalunya in Barcelona, Spain. The flume is 100 m long and 3 m wide, in which a sediment bed with an initial slope of 1:15 was built. This bed consists of medium sand with sand characteristics $D_{50} = 0.25\,\text{mm}$, $D_{10} = 0.15\,\text{mm}$ and $D_{90} = 0.37\,\text{mm}$. The mean sediment settling velocity was measured as $w_s = 0.034\,\text{m/s}$.

The waves were generated as a first order bichromatic wave with two wave components. The wave group period was $T_{gr} = 14.8\,\text{s}$ with a wave repetition period $T_r = 2T_{gr}$, meaning that every repetition consisted of two different wave groups. The individual wave components had periods $T_1 = T_r/7$ and $T_2 = T_r/9$ and wave heights $H_1 = H_2 = 0.32\,\text{m}$. Together the wave components have a mean short wave period of $T_m = T_r/8 = 3.7\,\text{s}$. Reflected waves that travel back to the paddle were not absorbed in the lab experiment. This is different in the numerical model where the reflected waves are absorbed by the relaxation zone. This is expected to result in slightly different wave conditions (Van der A et al., 2017).

The measurements featured an array of measuring equipment. The full description can be found in the original paper of Van der Zanden et al. (2019a). In this study we use the acoustic wave gauges, the ADV probes for measuring flow velocities and OBS probes for measuring sediment concentrations. Fig. 1 shows the location of the instruments. The OBS and ADV probes were mounted 3 cm above the bed at the start of the wave run.

2.2. Model description

We use the model of Kranenborg et al. (2022), which was adapted from the model of Jacobsen et al. (2014), to use in the swash zone. Although the model is capable of morphodynamic simulations, in this study we limit ourselves to modelling suspended sediment transport only and not take intraswash morphodynamics into account. In other words, we run the model using a static bed but still allow suspended sediment to entrain and settle.

The model is defined on a 2D spatial domain $D \subset \mathbb{R}^2$, where we define the Cartesian coordinates in two notations, $(x_1, x_2) = (x, y)$, with its origin at the still water line and positively directed towards the beach and up respectively. Throughout the paper we use the x and y coordinates for analysis, but for the description of the model equations we use Einstein notation. t refers to the time coordinate. In total, we run the simulations from $t_0 = 30\,\text{s}$ to $t_{end} = 240\,\text{s}$. This is because the paddle was stationary for the first 30 s.

2.2.1. Implementation

The model solves the 2DV incompressible RANS equations and uses the Volume of Fluid (VoF) method for discriminating between air and water. Specifically, we use the isoAdvector approach of Roenby et al. (2016). This introduces a volume fraction field α with which in each cell fluid properties ψ are set using

$$\psi = \alpha\psi_{water} + (1-\alpha)\psi_{air}. \tag{1}$$

To close the flow equations we use the $k{-}\omega$ turbulence model, incorporating the Wilcox (2006) and Larsen and Fuhrman (2018) limiters, defined here in Einstein notation following the conventions of Larsen and Fuhrman (2018):

$$\frac{\partial \rho k}{\partial t} + \frac{\partial \rho u_j k}{\partial x_j} = 2\nu_t S_{ij} S_{ij} - \rho\beta^* k\omega + \frac{\partial}{\partial x_j}\left(\mu + \rho\sigma^* \frac{k}{\omega}\frac{\partial k}{\partial x_j}\right), \tag{2}$$

$$\frac{\partial \rho \omega}{\partial t} + \frac{\partial \rho u_j \omega}{\partial x_j} = \alpha_\omega 2\frac{\omega}{\tilde{\omega}} S_{ij} S_{ij} - \rho\beta\omega^2 + \rho\frac{\sigma_d}{\omega}\frac{\partial k}{\partial x_j}\frac{\partial \omega}{\partial x_j} + \frac{\partial}{\partial x_j}\left(\mu + \rho\sigma\frac{k}{\omega}\frac{\partial \omega}{\partial x_j}\right), \tag{3}$$

k being the turbulent kinetic energy density and ω being the specific dissipation rate. The mean strain rate tensor is defined as

$$S_{ij} = \frac{1}{2}\left(\frac{\partial u_i}{\partial x_j} + \frac{\partial u_j}{\partial x_i}\right), \tag{4}$$

with u_i and x_i are the velocity and spatial coordinate components. ρ is the density, μ and ν are the dynamic molecular viscosity and the kinematic viscosity respectively, which all depend on the volume fraction field α. Furthermore, $\beta = 0.708$, $\beta^* = 0.09$, $\sigma^* = 0.6$, $\sigma_{do} = 0.125$, $\sigma = 0.5$, $\alpha_\omega = 0.52$ and

$$\sigma_d = H\left(\frac{\partial k}{\partial x_j}\frac{\partial \omega}{\partial x_j}\right)\sigma_{do} \tag{5}$$

are all model parameters (with H being the Heaviside step function). Here the turbulent eddy viscosity ν_t is defined as

$$\nu_t = \frac{k}{\tilde{\omega}}. \tag{6}$$

It remains to define the two limited versions of ω:

$$\tilde{\tilde{\omega}} = \max\left(\omega, \lambda_1\sqrt{\frac{p_0}{\beta^*}}\right), \quad \tilde{\omega} = \max\left(\tilde{\tilde{\omega}}, \lambda_2 \frac{\beta}{\beta^*\alpha}\frac{p_0}{p_\Omega}\omega\right), \tag{7}$$

where $p_0 = 2S_{ij}S_{ij}$, $p_\Omega = 2\Omega_{ij}\Omega_{ij}$, with

$$\Omega_{ij} = \frac{1}{2}\left(\frac{\partial u_i}{\partial x_j} - \frac{\partial u_j}{\partial x_i}\right). \tag{8}$$

Following Larsen and Fuhrman (2018) we use $\lambda_2 = 0.05$ and $\lambda_1 = 0.875$ by default. Later in the paper, the (Wilcox, 2006) limiter will be deactivated by setting $\lambda_1 = 0$.

We do not apply a buoyancy production term as this can lead to stability issues around wave-breaking and it does not lead to considerable differences in modelled morphodynamics (Christoffersen, 2019). The effects of sediment on turbulence are not accounted for in this model. For wave generation we use the waves2Foam module (Jacobsen et al., 2012), coupled with OceanWaves3D (OW3D) (Engsig-Karup et al., 2009; Paulsen et al., 2014).

We model suspended sediment transport using an advection diffusion approach where the evolution of the sediment concentration field c is modelled as

$$\frac{\partial c}{\partial t} + (\alpha u_i + w_s\delta_{i3})\frac{\partial c}{\partial x_i} - \frac{\partial}{\partial x_i}\left[\alpha(\nu + \nu_t)\frac{\partial c}{\partial x_i}\right] = 0, \tag{9}$$

where δ_{i3} is the kronecker delta and the sediment is advected by the sum of the flow velocity and the fall velocity w_s, which is calculated following the method of Fredsøe and Deigaard (1992). Sediment is diffused by the sum of the fluid kinematic viscosity and the eddy viscosity ν_t. For details of the implementation we refer to the initial publication on the model by Jacobsen et al. (2014).

2.2.2. Model geometry and mesh

Fig. 1 shows the setup of the model, consisting of different zones where different models are run. The full model domain, reaching from the seaside to above the swash, is 87 m long. At the seaward side, the water depth is $h_0 = 2.5$ m. As written above, the full model consists of two different models that are coupled together using a relaxation zone. The OW3D model is run on the full domain, from the seaward boundary at $x_p = -75.97$ m up to $x = 11.03$ m. The domain of the depth-resolving OpenFOAM model starts at $x = -50.47$ m and reaches to $x = 11.03$ m at the upper swash boundary. The region between $x = -50.47$ m and $x = -41.97$ m defines the relaxation zone where the solution of OW3D is mapped onto the depth-resolving model. Details about the relaxation zone method and the mapping can be found in Jacobsen et al. (2012).

The geometry of the depth-resolving model domain follows the measured bed profile before the experiment run took place (see Section 2.1 below). The profile was measured from approximately $x = -22.3$ m upward. The profile offshore from this point was assumed to be linear with a slope of 1:15 until the toe of the profile at depth $y = -h_0$. The domain height generally is 3.3 m, except at the sloped section where the top of the domain is a straight line, with endpoints 3.3 m above the bottom profile.

The mesh is created by rectangular cells with a cross-shore length of 4 cm. The vertical discretisation is done in three layers. This is done to facilitate a high resolution at the bed boundary while keeping the aspect ratio small in the majority of the domain. The bottom layer is 10 cells thick with all cells being 0.625 mm thick. This layer follows the bed geometry. The top layer is 2.3 m thick and consists of 140 cells with the same thickness (approximately 16.4 mm). This layer follows the top, linear boundary geometry. The middle layer, consisting of 177 cells, facilitates a smooth transition between the two outer layers.

The OW3D model is discretised in 1000 equidistant points in the x-direction.

2.2.3. Boundary conditions and wave generation

The boundary conditions are very similar to the (Kranenborg et al., 2022) study, with no-slip boundary conditions at the bed, offshore and onshore boundaries, and an ambient atmospheric pressure condition at the top boundary, from which the velocity condition is calculated. We use the (Fuhrman et al., 2010) boundary conditions for k and ω at the bed. We use the (Cebeci and Chang, 1978) rough wall model, implemented by Larsen et al. (2017) for modelling the friction velocity and incorporating the bed roughness. For this we use a Nikuradse roughness height of $k_N = 2.5D_{50}$, where D_{50} denotes the median grain size.

For sediment transport we use the (Zyserman and Fredsøe, 1994) reference concentration to determine the suspended sediment concentration c at the reference height $y_a = 2.5D_{50}$ above the bottom boundary. Here we also use the new divergence scheme proposed in Kranenborg et al. (2022) to stabilise the sediment concentrations at the boundary, mitigating wiggles and negative sediment concentrations (Jacobsen, 2011). The (Zyserman and Fredsøe, 1994) approach requires the Shields parameter θ as input, which we here define as

$$\theta = \frac{|\tau_b|}{(\rho_s - \rho)gD_{50}}, \tag{10}$$

where τ_b is the bed shear stress as calculated using the turbulence model, $\rho_s = 2650\,\mathrm{kg/m^3}$ is the sediment density, ρ is the fluid density and $g = 9.81\,\mathrm{m/s^2}$ is the magnitude of the gravitational acceleration. We here define the Shields parameter to always be positive.

We generate the waves at the offshore boundary in the domain. Similar to Chen et al. (2022), Jacobsen et al. (2018), we apply the OW3D model to incorporate the paddle velocity signal. In our study, we do not use the paddle velocity signal u_p directly but modify it by a scaling factor γ_p to create the model paddle velocity u_p^m:

$$u_p^m = \gamma_p u_p. \tag{11}$$

This is because the paddle in the experiments is of the wedge type, which has is different from the model paddle in two important ways. For one, the laboratory paddle has a vertical component in its stroke movement where the model paddle only allows horizontal movement. Secondly, because of the nonhorizontal paddle stroke, the laboratory paddle does not contact the water for the full flume depth h_0, which is the case in the model. The calibration process was done by comparing modelled surface elevations using paddle signals produced by a gamma varying between 1 and 0.7, with an interval of 0.05. In the end, $\gamma_p = 0.75$ gave the best results. We do not give more details on this calibration here, but refer to the general model verification in Section 3.

The OW3D model assumes a constant depth of h_0, and as such does not include the bottom geometry (see Fig. 1). This is not an issue for offshore generated waves, as the coupling between the models is done before the toe of the bed profile. However, waves reflected in the OW3D model would be different because of the different bed profiles between the OW3D and depth-resolving models. Therefore, the OW3D model has a damping zone which absorbs the offshore generated waves after the coupling region.

2.3. Model verification

To aid in verification of the model performance, a normalised Root Mean Square Error (nRMSE) is calculated for the water surface, flow velocities and the sediment concentrations. For the free surface location we use the deviation from the initial water depth η. For the flow velocity comparison, the normalisation variable is the maximum of the absolute value of the measured velocity. Furthermore, dry periods in the measurement data (measurements were done at 3 cm above the bed) were removed from the data before comparison. The latter point also holds true for comparisons of sediment concentration. We also note that there were no co-located measurements of velocities and concentrations. As such the model predictions of the vertical distribution of sediment and velocity cannot be verified.

2.4. Analysis of cross-shore fluxes

To calculate the advective cross-shore flux F at a certain position we integrate the local sediment transport flux. This is done in the following manner:

$$F = \int_{y_b+y_a}^{y_{top}} c(y)u_x(y)\mathrm{d}y, \tag{12}$$

where $c(y)$ and $u_x(y)$ describe the suspended sediment concentration and the cross-shore velocity at depth y. Here y_b is the bed level, y_a is the reference height used for the suspended sediment boundary condition and y_{top} is the upper bound of the domain at the particular cross-shore location. The integration bounds include parts of the domain that are filled with air. This avoids dealing with cases where the free surface is not easily defined such as overturning waves or bubbles in the flow. Also, because the air is free from sediment, it does not contribute to the transport integral.

As a proxy for depth-averaged models, we can similarly define a flux F_u by first averaging the velocity and integrating the sediment concentration over depth:

$$F_u = UC, \tag{13}$$

where U is defined as

$$U = \frac{1}{h - y_a}\int_{y_b+y_a}^{y_{top}} u_x(y)\alpha(y)\mathrm{d}y, \tag{14}$$

with α being the volume fraction of air and water, and the water depth h defined as

$$h = \int_{y_b}^{y_{top}} \alpha(y)\mathrm{d}y, \tag{15}$$

and the depth integrated concentration C is defined as

$$C = \int_{y_b+y_a}^{y_{top}} c(y)\mathrm{d}y. \tag{16}$$

Note that for ease of comparison, both fluxes are calculated in the suspension part of the domain only.

We then define the difference between these fluxes as

$$\Delta_F = F - F_u, \tag{17}$$

which means Δ_F can be interpreted as the signed remainder of the flux that is needed when modelling the flux assuming vertically uniform sediment and velocity distributions.

Depth-averaged models that model suspended sediment transport often employ a similar advection diffusion model where sediment is transported using the flow velocity. However, because of vertical nonuniformities, one could use a different velocity U_c, here called the effective transport velocity, as the advection velocity in the transport equation. Using this, we can redefine the depth-averaged flux given in Eq. (13) by substituting the depth-averaged velocity U with the effective transport velocity U_c and equate it to the flux defined in Eq. (12):

$$U_cC = F \iff U_c = \frac{F}{C}. \tag{18}$$

This gives us a way to analyse the effective transport velocity in a depth-averaged approach, in terms of the depth-integrated sediment concentration and the depth-resolved sediment flux. Note that for small water depths this equation becomes very sensitive due to C being close to zero. For this reason, both fluxes and the effective transport velocity are assumed to be zero when the water depth is lower than 0.5 cm.

We define the difference between the velocities Δ_U as

$$\Delta_U = U - U_c. \tag{19}$$

It is important to note that, while we use the above defined metrics as methods to compare with a depth-averaged, or depth-uniform, approach, the calculation of F_u is still based on the depth-resolving model. These assumptions and their impact on the interpretation of the analyses using this is further discussed in Section 5.4

For all integrals above the numerical integration is achieved using the trapezoidal method.

In the remainder of the manuscript, time-averaging over a time interval T is denoted as $\langle . \rangle_T$.

Table 1
The definitions of the four different model configurations.

Config	Wilcox (2006) limiter	Bubble modification
A	on	off
B	on	on
C	off	off
D	off	on

3. Model improvements and verification

This section deals with the model verification and the steps to improve the performance. Before going into detail about the results, we provide a quick background to give the reader some context before we dive into the issues discovered and the solutions found.

The starting point is the (Kranenborg et al., 2022) model. However, when analysing the model results we quickly noticed that air bubbles would stick to the bed. These bubbles led to underpredicted friction and sediment transport, particularly in the uprush. Section 3.1 explains this issue in more detail and proposes a temporary solution, here called the bubble modification.

A second issue found was that the prediction of suspended sediment concentrations was insufficient. More specifically, very little sediment was brought into suspension in the lower swash during uprush. Furthermore, when a suspension event happened it was very localised and short-lived. One important parameter contributing to the capacity of the flow to carry sediment is the eddy viscosity ν_t. For this reason, the influence of the (Wilcox, 2006) limiter in the turbulence model was analysed. The results of this analysis is written in Section 3.3.

These two issues are treated separately because, as will be detailed below, they have different origins. These two modifications lead to four different model setups, as detailed in Table 1. The effect of the different configurations on sediment transport is shown in Section 3.4. Finally, the verification of the best model configuration is detailed in Section 3.5.

3.1. 2DV bubble effects

The model does not describe the air/water interface directly, instead it uses a VoF approach for bookkeeping whether individual cells contain water or air. This enables the modelling of more complex surface interface shapes that, for instance, a model based on the shallow water equations cannot capture. One result of this is that bubbles can be formed. In our case, this leads to the model trapping air below the swash. Fig. 2 shows what happens both at the swash tip and the same location roughly two seconds later. As the swash moves up the beach, sometimes small pockets of air get trapped below the swash flow.

A possible explanation is the phenomenon of numerical ventilation. This phenomenon has previously been seen in simulations of planing ship hulls (e.g. Viola et al., 2012; Mancini et al., 2016; Gray-Stephens et al., 2019). Numerical ventilation is the phenomenon where the numerical discretisation of the VoF field α leads to an unphysical layer of air sticking to a body. For planing hulls this layer of air forms at the triple point between the air phase, the water phase and the hull. For more details on numerical ventilation, we refer to Gray-Stephens et al. (2019). Apart from numerical ventilation, once bubbles have formed, bubbles do not rise as quickly in a 2DV simulation compared with a 3D simulation. This is further detailed in Appendix A.

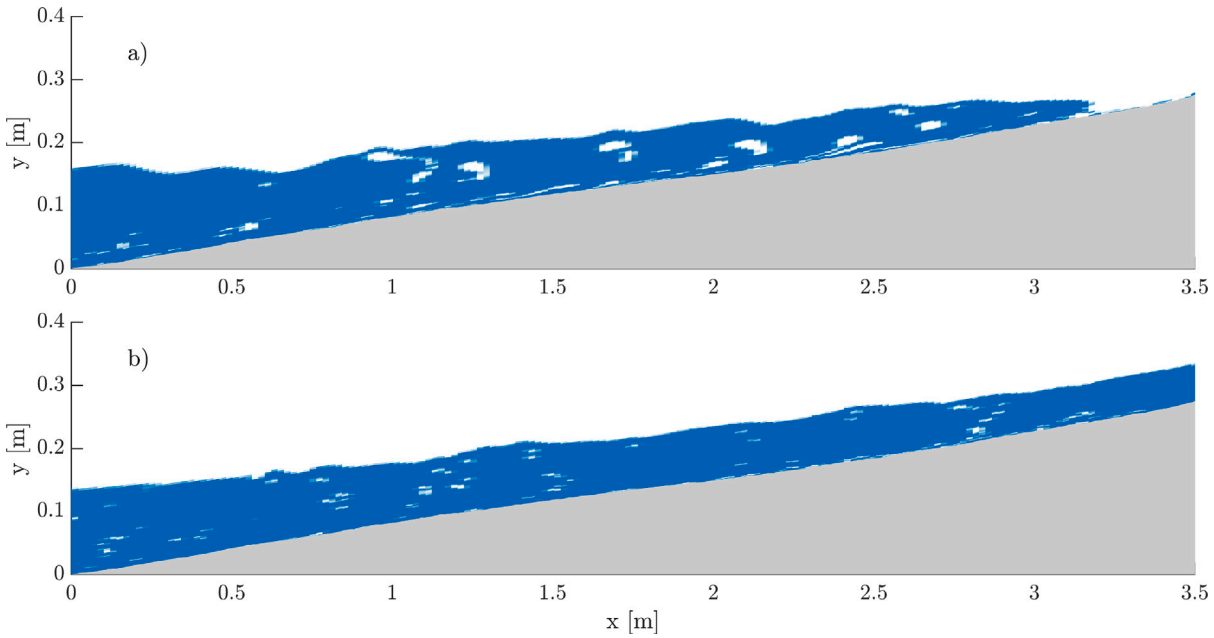

Fig. 2. Figure showing the volume fraction field α between $x = 1\,\text{m}$ and $x = 3.5\,\text{m}$ at $t = 167.4\,\text{s}$ (a) near the swash tip during uprush and at $t = 169.3\,\text{s}$ (b) roughly two seconds after the swash tip has passed, exemplifying the issue with air content near the bed.

Fig. 3 shows the modelled density at the bed ρ, friction velocity u_*, surface elevation η and Shields parameter θ in time and space. The friction velocity is related to the shear stress as

$$u_* = \frac{\tau_b}{|\tau_b|}\sqrt{\frac{|\tau_b|}{\rho}}. \tag{20}$$

Note that the friction velocity incorporates the direction of the shear stress, whereas the Shields parameter does not. During uprush, easily identified by the positive i.e. onshore friction velocity, the bed density shows very patchy behaviour with regions where the density is low, for instance at $x = 4\,\text{m}, t = 165\,\text{s}$ (here low means close to air density: $\rho \approx 1\,\text{kg/m}^3$). In terms of the Shields parameter, the uprush also shows patchy behaviour and higher values only very localised. This is in stark contrast with the behaviour during the backwash, which displays a large patch in space and time with high Shields values.

3.2. Modification to remove bubbles

To investigate the impact of these bubbles, a modification to the model is introduced. This modification aims to remove bubbles that are considered unphysical. This is the case when two criteria are met simultaneously, namely that bubbles are within a distance d_b from the bed, and that the total pressure at that location is higher than P_b. This last criterion can be thought of as a distance to the free surface, where the pressure is roughly 0 Pa. Combining these criteria means that we remove bubbles that are close enough to the bed but far enough from the free surface. In other words, bubbles may be present around wave-breaking, bores or at the swash tip, but if they linger at the bed they will be removed. This is similar to method of adding a source term to the VoF model, a commonly used strategy to mitigate numerical ventilation in planing hull simulations (Viola et al., 2012; Mancini et al., 2016; Gray-Stephens et al., 2019).

The procedure to remove bubbles is straightforward. For every cell in the model that meets the criteria mentioned above, the value of α is checked. This value is then set to $\alpha = 1$, meaning the cell is forced to contain water. This means that the modification works by adding water to the model. In Section 5.1 the impact of this method, and other potential methods of dealing with bubbles in 2DV models are discussed.

The modification is applied in configurations B and D using the criteria $d_b = 0.05\,\text{m}$ and $P_b = 500\,\text{N/m}^2$, which corresponds to a surface elevation of roughly 5 cm. Fig. 4 shows the results using this model (configuration B). The results are very different from the results presented where the bubbles were not removed (compare with Fig. 3). In this case, the density is almost always close to $\rho = 1000\,\text{kg/m}^3$ underneath the submerged parts of the beach. Furthermore, the friction velocity and Shields parameter now do not display the patchiness during the uprush. Also, the magnitude of the Shields parameter has increased during uprush and decreased during the backwash. The effect on sediment transport will be shown in Section 3.4.

3.3. Turbulence effects

To analyse the quality of sediment predictions by the model we compare them to the measurements of the OBS probes. Fig. 5 shows the time series of the modelled sediment concentrations for all four configurations. It shows that for Configuration A, the concentrations do not correspond at all with the time series of the measured concentrations. Especially at the upper two locations, the model underestimates the magnitude of the sediment concentration during uprush (see especially panels (b–e) at $t = 137\,\text{s}$ and $t = 153\,\text{s}$). Furthermore, especially at locations (b) and (c), the model predicts high concentrations at the end of the backwash around $t = 163\,\text{s}$.

As turbulence is an important factor in both the pick up of sediment and the ability for the flow to hold sediment in suspension, it is natural to look at how modifications to the turbulence modelling can influence the results. Eqs. (3) and (7) show that a low value of λ_1 leads to a lower specific dissipation rate ω, i.e. slower dissipation of k. Larsen and Fuhrman (2018, Figure 6) also show that the limiter of Wilcox (2006) has a large impact on the eddy viscosity from the point of wave-breaking for spilling breakers (Ting and Kirby, 1994). Specifically, with the limiter turned off, i.e. $\lambda_1 = 0$, the eddy viscosity was notably higher after the waves had broken. However, when this turbulence model was used, the model became unstable when, during the process of wave-breaking, the overturning wave shape was about to touch the water surface below. Here, a layer of air was trapped between the two approaching water surfaces. In this thin air layer, the turbulent kinetic energy, and thus the eddy viscosity, rapidly increased. This

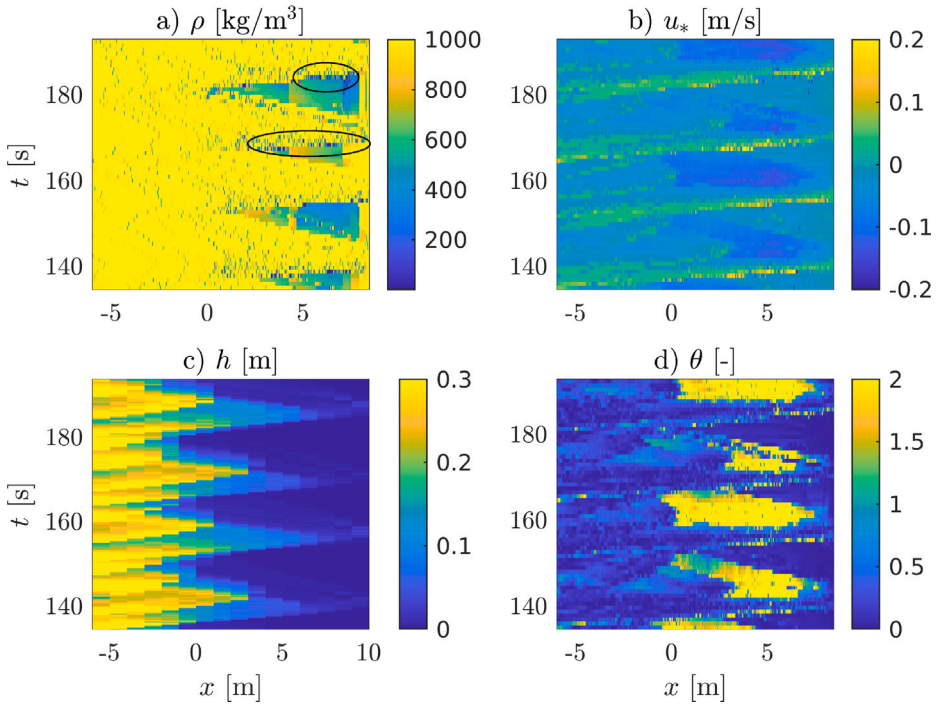

Fig. 3. Time series of the spatial variation in (a) density at the bed, (b) friction velocity u_*, (c) water depth h and (d) Shields parameter θ from a simulation using with no bubble or turbulence modifications (Configuration A, Table 1). The circles in panel (a) show examples or regions where the density is low due to the presence of air at the bed below the uprush flow.

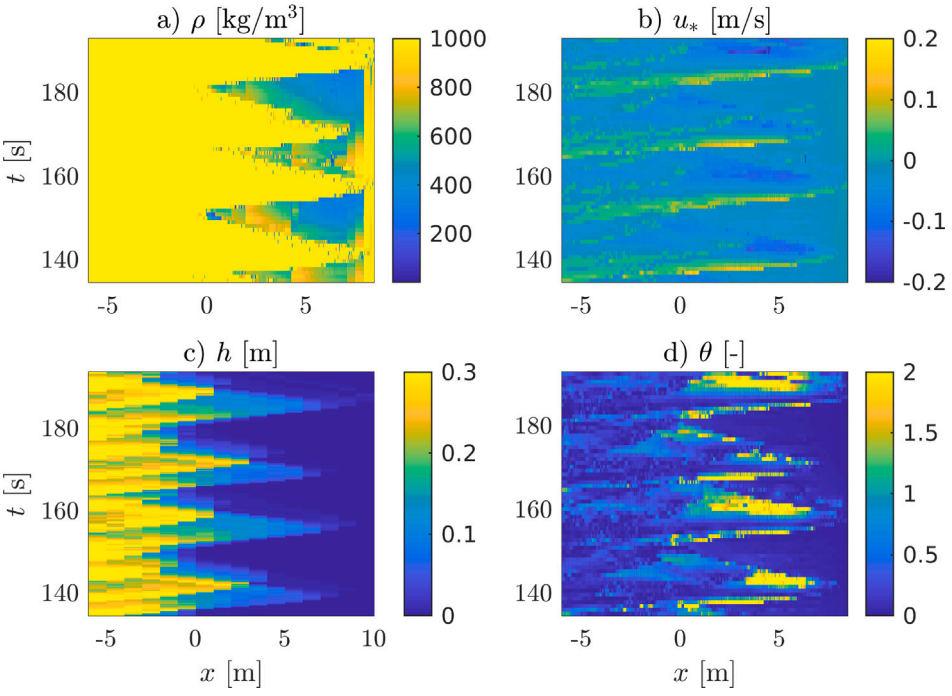

Fig. 4. Time series of the spatial variation in (a) density at the bed, (b) friction velocity u_*, (c) water depth h and (d) Shields parameter θ from a simulation using Configuration B (Table 1).

destabilised the solution, leading to unphysically high flow velocities, eddy viscosities, pressures and eventually a model crash. To mitigate this, the turbulence production term $2\nu_t S_{ij} S_{ij}$ in Eq. (2) was deactivated in the air phase by multiplying it with α.

The impact of the limiter and bubble modification can be seen in Fig. 6, where the instantaneous spatial distribution of the cross-shore velocity u_x, the suspended sediment concentration c and the turbulent kinetic energy k are shown during an uprush. Here, configurations A and B with the (Wilcox, 2006) limiter active, i.e. where $\lambda_1 = 0.875$, display considerably lower levels of turbulent kinetic energy (panels (i) and (j)) compared to configurations C and D, where the limiter is inactive (panels (k) and (l)). This is also seen in the sediment

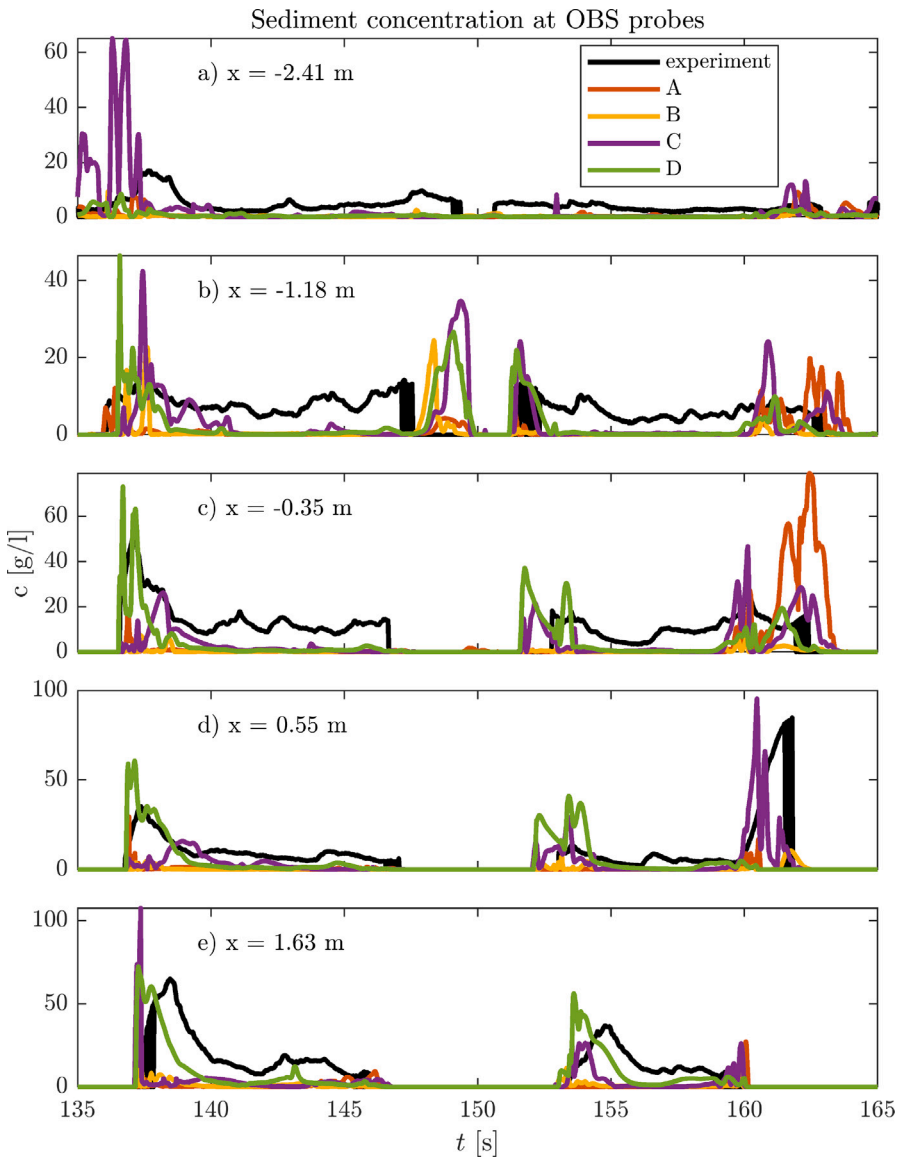

Fig. 5. Comparison of suspended sediment concentration at the location of the OBS probes, 3 cm above the bed, for the four different model configurations. Here the measured concentrations are only shown for times when the water depth is larger than 5 cm. This figure shows two swash events.

concentration field, which shows higher suspension levels at the swash tip when the limiter is deactivated (see panels (g) and (h), between $x = -2$ m and $x = 0$ m).

3.4. Effect on sediment transport

Fig. 5 shows that there are large differences in the modelled sediment concentration behaviour between the model configurations. Configurations A and B generally show low sediment concentrations, except at the end of the backwash in panels (b) and (c). Compare this to the model configurations C and D where $\lambda_1 = 0$, which generally produce higher concentrations in the uprush. Furthermore, a comparison between configurations C and D shows that bubble modification leads to increased sediment concentrations for the more onshore locations (panels (c–e)), suggesting that numerical ventilation and bubbles lead to lower shear stress predictions. This seems to be especially important at the beginning phase of the uprush (e.g. $t = 137\,s$). Both the limiter and the near-bed bubbles lead to lower concentrations in the uprush, which is explained by a lowering of the shear stress. A decreased shear stress in the uprush phase also means that more energy is conserved, making the backwash stronger. This explains the relatively high sediment concentrations during the backwash predicted by configurations A and C at $t = 162$ s.

Fig. 7 shows time-averaged flow velocities and cross-shore sediment fluxes for all model configurations. The hydrodynamics are qualitatively very similar, displaying only minor differences, for instance around the point of wave-breaking (see B for a comparison of wave gauges and flow velocities between Configurations A and D). However, there are apparent differences in the averaged suspended sediment flux. Most clearly, the direction of transport in the swash has changed from offshore for configuration A to more onshore, especially for configurations B and D. This can be explained by a combination of two effects. First, the presence of bubbles decreases the bed shear stress resulting in lower reference concentrations. Furthermore, the bubbles inhibit the pickup of sediment even when the reference concentration is large. This is because the sediment diffusion term in Eq. (9) becomes zero in air where $\alpha = 0$. This makes the suspended sediment transport in Configurations B and D comparatively much stronger in the uprush. At the same time, the extra friction during the uprush means that the swash has lost energy, which explains the weaker backwash. The combination of these effects mean that, where the model configuration

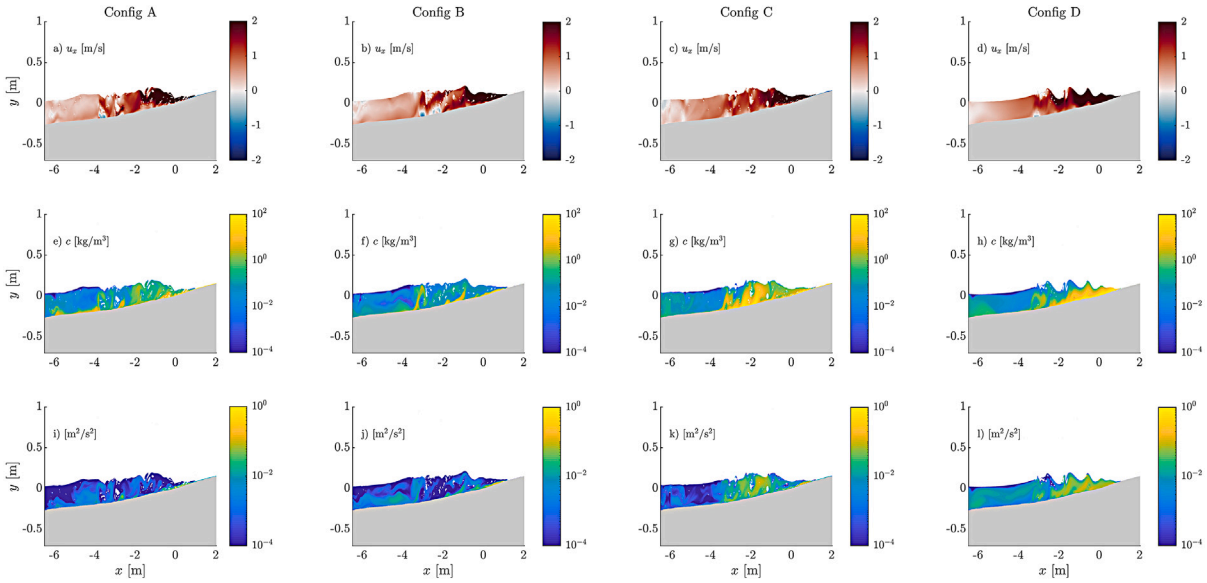

Fig. 6. Figure showing (a, b, c, d) cross-shore flow velocities, (e, f, g, h) suspended sediment concentrations c and (i, j, k, l) turbulent kinetic energy density k for four different configurations during the uprush at $t = 137$ s.

Table 2
nRMSE values of sediment concentration time-series of the five configurations compared with the measurements. The nRMSE is calculated for $T \in [135\,\text{s}, 135 + 3T_r\,\text{s}]$, i.e. three group repetitions, and is only calculated for points in time where measurement data exists. Here the columns correspond to the five locations and panels in Fig. 5, and the rows correspond to the four model configurations.

	1, (a)	2, (b)	3, (c)	4, (d)	5, (e)
A	0.172	0.269	0.301	0.185	0.332
B	0.162	0.249	0.248	0.143	0.223
C	0.213	0.245	0.237	0.132	0.218
D	0.167	0.221	0.222	0.150	0.208

A predicts offshore transport in the swash, model configuration B predicts onshore transport. In other parts of the domain the differences are smaller, which is expected as the impact of bubbles was already small outside of the swash zone. A similar argument can be made for configuration C and D. The (Wilcox, 2006) limiter leads to decreased levels of turbulence. Therefore, in configurations C and D, turbulence levels are higher and in turn friction is higher, leading to increased sediment transport. Configuration D combines both effects that increase friction during the uprush, which explains why this leads to the most onshore sediment transport.

To confirm the visual inspection, Table 2 shows normalised Root Mean Square Errors (nRMSE) for all configurations at the five different OBS locations. Configuration D overall scores the best, having the lowest nRMSE at three locations. Only at locations 1 and 4 do other configurations perform better. Looking at Fig. 5, the relatively good performance of configuration C at location 4 can be explained by the backwash peak around $t = 160$ s. This backwash peak is dominant in the data. For the first location, panel a), all configurations underpredict the concentration in a similar fashion, except Configuration C, and as such the difference in performance of configurations A, B and D is small.

From the results discussed above we conclude that model configuration D results in the best modelled sediment behaviour. This is the model configuration that will be used for the remaining analysis in this paper. We emphasise that this is only based on point measurements of the sediment concentration and that the predicted vertical distribution of sediment concentration and velocities are not verified.

3.5. Final model verification

It remains to show the hydrodynamic performance of the model. As determined in Section 3.4, model configuration D overall reproduces the suspended sediment dynamics the best. Therefore, the hydrodynamic verification will only be presented for that model.

Fig. 8 shows a comparison of the surface elevation time series. These are complemented with nRSME values in Table 3. At the three most offshore locations, the waves have not broken yet. Here, the model predicts the surface elevations very well, capturing the amplitude and shape of the waves. The largest discrepancies happen in between the wave groups where the group envelope is small. These discrepancies become smaller as the waves transform when they travel further in the flume. At the last probe location before wave breaking ($x = -13.99$ m), the modelled waves still correspond well to the measurements. Between this probe and the next probe at $x = -6.3$ m, the waves break. This is evident in the signal at this next probe, which is very spiky for both the measured and the modelled signals. The next two probes (at $x = -4.17$ m and $x = -1.25$ m) show the surface elevation in the surf zone, offshore of the initial water line. Here intermittent effects from wave-breaking and possibly air bubbles lead to some differences in the details between the measured and modelled signals. However, the overall behaviour is well reproduced, with the two alternating wave groups showing distinct behaviour at the upper two probe locations (at $x = 0.52$ m and $x = 2.77$ m). However, especially at the upper most probe, the differences become larger. Also, at $x = 0.52$ m, the probe measures negative surface elevations at the experiments, which points to local erosion happening. This will be further discussed in Section 5.3.

Similarly, we compare the cross-shore flow velocities in Fig. 9, for five locations around the initial water line, and at 3 cm above the bed. nRMSE values of these time-series can be seen in Table 4. Again, the model predicts the measured velocities very well. The model does show somewhat higher peak velocities at $x = -1.25$ m and $x = -0.46$ m, but the general behaviour is still captured well. Above the still water line, the ADV measurements become unreliable when exposed to the air. Also, at the start of wet periods the signal is spiky and might be unreliable due to the ADV needing some time to adapt when being wetted. During the wet periods, the model predicts the velocities very well, capturing even some minor details in the flow at for instance $t = 160$ s.

Overall, we conclude that the model performs well hydrodynamically. We discuss this further in Section 5.3.

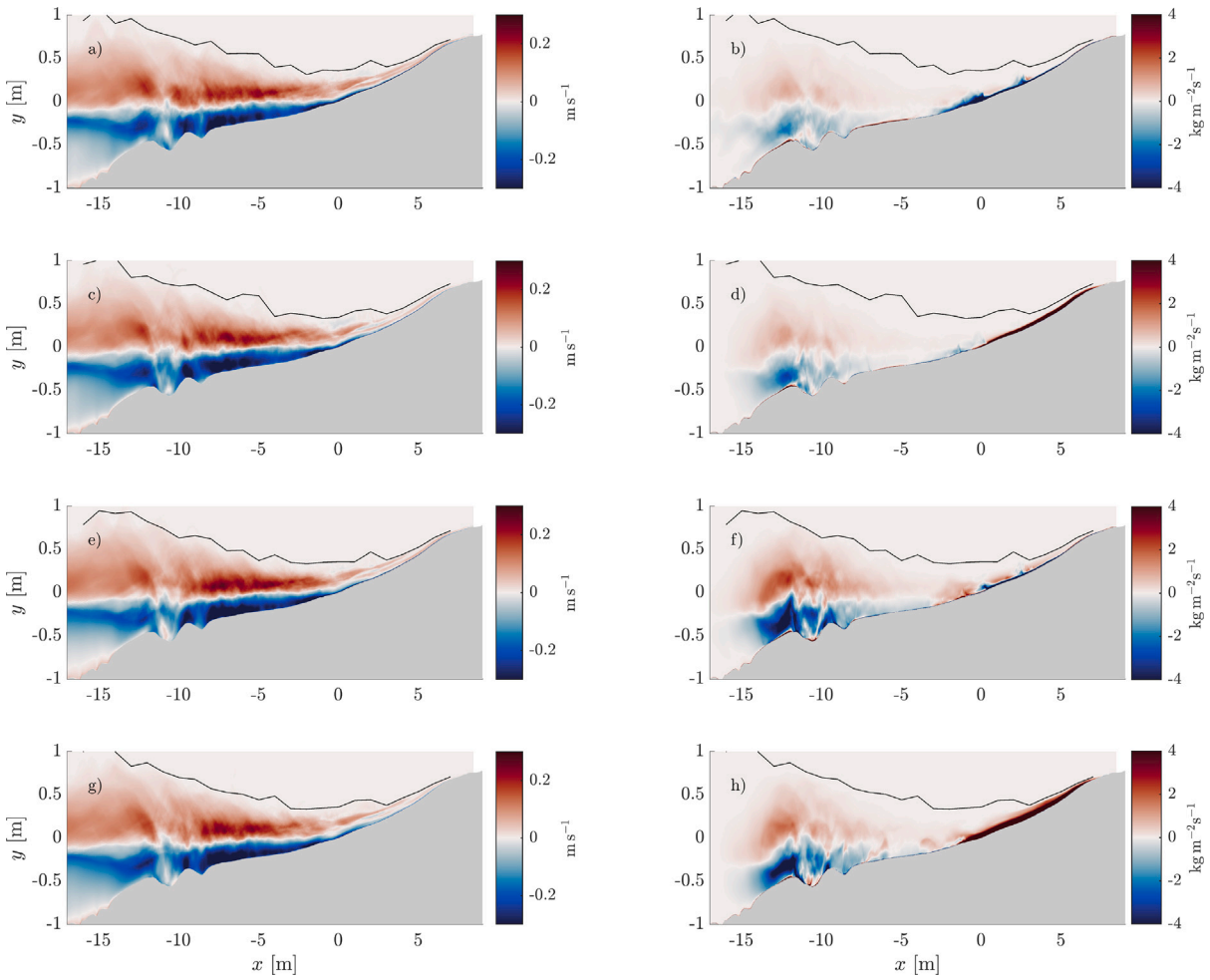

Fig. 7. Figure showing the time-averaged cross-shore velocity in the water phase (a, c, e, g) and time-averaged cross-shore suspended sediment flux (b, d, f, h) in a region of the domain D for three wave repetition periods starting at $t = 120$ s. Panels (a, b) show the results using model configuration A, (c, d) show configuration B, (e, f) show configuration C and (g, h) show configuration D. The black line shows the envelope of the maximum surface elevation as defined in (15).

Table 3
nRMSE values of modelled deviations from the initial water depths (η) at eight different cross-shore locations. The nRMSE values are calculated for $T \in [135\,\text{s}, 135 + 3T_r\,\text{s}]$, i.e. three group repetitions, and is normalised by the maximum measured value.

x [m]	−45.67	−21.28	−13.99	−6.3	−4.17	−1.25	0.52	2.77
nRMSE	0.155	0.094	0.143	0.207	0.211	0210	0.127	0.129

Table 4
nRMSE values of modelled flow velocities 3 cm above the bed at five different cross-shore locations. The nRMSE values are calculated for $T \in [135\,\text{s}, 135 + 3T_r\,\text{s}]$, i.e. three group repetitions, and are normalised by the maximum measured (absolute) velocity.

x [m]	−2.27	−1.25	−0.46	0.55	1.53
nRMSE	0.536	0.357	0.369	0.465	0.537

4. Transport uniformity

The results of suspended sediment transport from the previous section, e.g. Fig. 7, show strong vertical dependence, at least when considering time-averaged suspended sediment fluxes. This section will go into more detail on the importance of these vertical dependencies.

Fig. 10 shows time series of the suspended sediment fluxes F and F_u, as well as cross-shore velocities U and U_c at five different cross-shore locations. Furthermore, the difference between the fluxes Δ_F is shown. The most offshore location coincides with the main breaker bar. Here, compared with the other two locations offshore of the initial water line, strong sediment transport occurs, and every peak in water depth coincides with a peak in onshore-directed suspended transport. In between the peaks, sediment is transported offshore. At the two other locations below the initial water line, only one prominent peak in the fluxes is visible, showing a momentary large onshore-directed sediment flux. At the two locations located onshore of the initial water line, two strong onshore-directed flux peaks that coincide with the arrival of the swash event are visible. Furthermore, the initial swash group shows a strong backwash flux, whereas the second swash group does not show as big a backwash flux.

The velocities U and U_c also show different behaviour at the different locations. At the most offshore location, both velocities U and U_c match well. This is an indication that the vertical sediment and velocity distribution is close to uniform, or at least that for the purpose of modelling the vertical distribution is not very important. Looking at the two other locations offshore of the initial water line, the lines generally coincide well but do differ at some points in time. For instance, during the local maxima in offshore transport, $|U_c| < |U|$, indicating that the uniform flux F_u overestimates the effective advection velocity. For the uprush, there is a moment at $x = -2.97$ m, roughly at $t = 152$ s where U_c is roughly half of U, indicating again that the uniform approximation

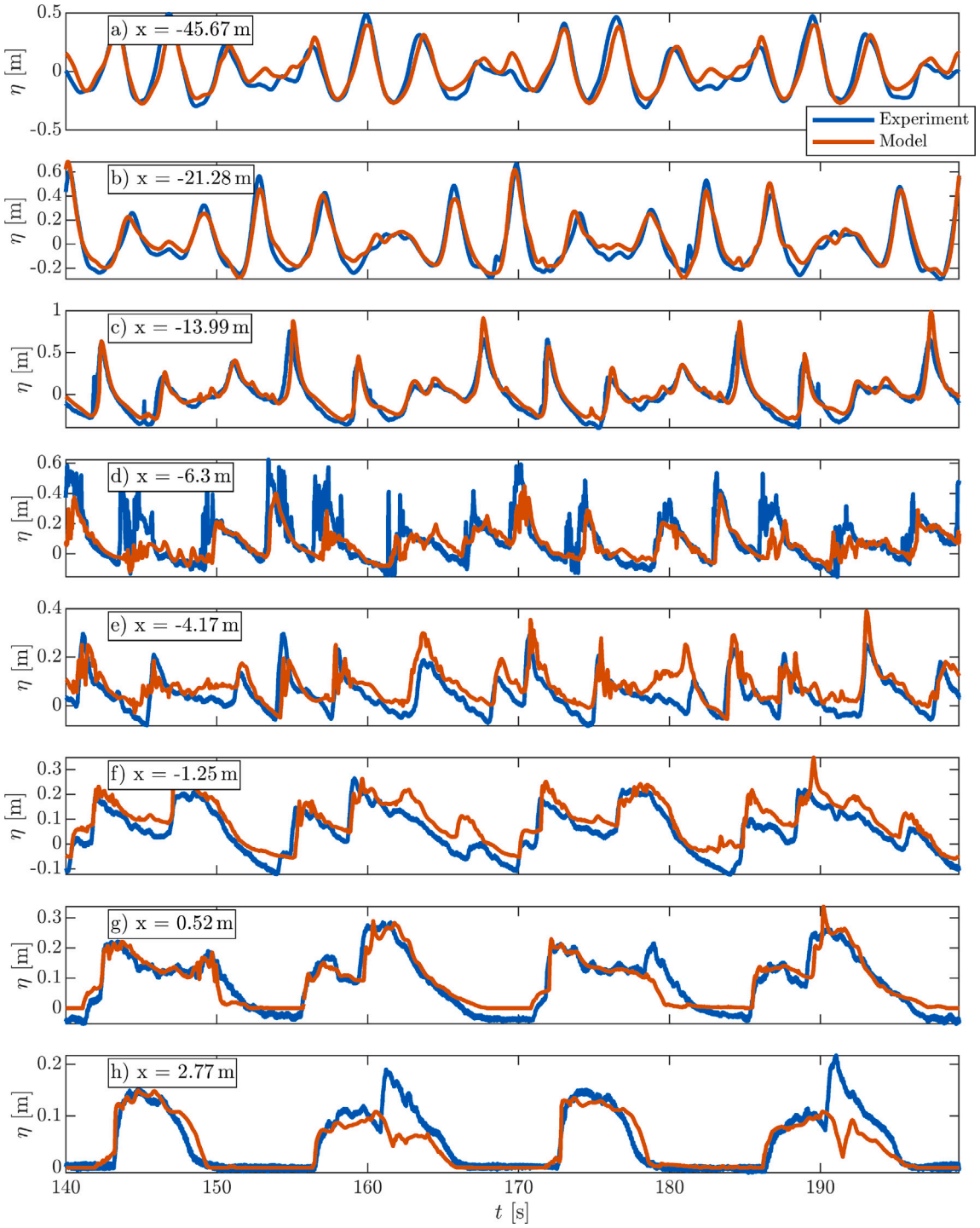

Fig. 8. Comparison between measured and modelled surface elevations at different locations, made using model configuration D.

would overestimate sediment transport. A similar overestimation happens after the bore at $t = 157$s, suggesting that bores can be a source of vertical nonuniformity in the sediment flux. The same characteristics are also seen at the two most onshore locations, although the difference is relatively small for the most onshore location.

We can also look at how time averages of the fluxes F, F_u and the difference Δ_F vary spatially. The time-averaged quantities, averaged over three repetition periods (T_r), are shown in Fig. 11. Here, the behaviour in the swash-zone stands out, showing overall large net onshore sediment fluxes. Here, the uniform approximation F_u leads to an overestimation of the onshore sediment flux. Another interesting observation is that when one first takes the absolute value of the difference Δ_F, the largest difference actually occurs at the position of wave-breaking, and not in the swash-zone as one might expect. This can be explained by looking at the instantaneous fluxes in Fig. 10, where at the point of wave-breaking Δ_F displays both a positive and negative error in time. Contrast this with the two upper locations, where Δ_F is mostly negative. Measuring the error in an absolute sense ensures that positive and negative errors do not cancel out, but it cannot tell the direction of the error. In short, although the differences are bigger at the point of wave-breaking, the net difference is substantially larger in the swash zone. In terms of uniformity in depth, again this points to

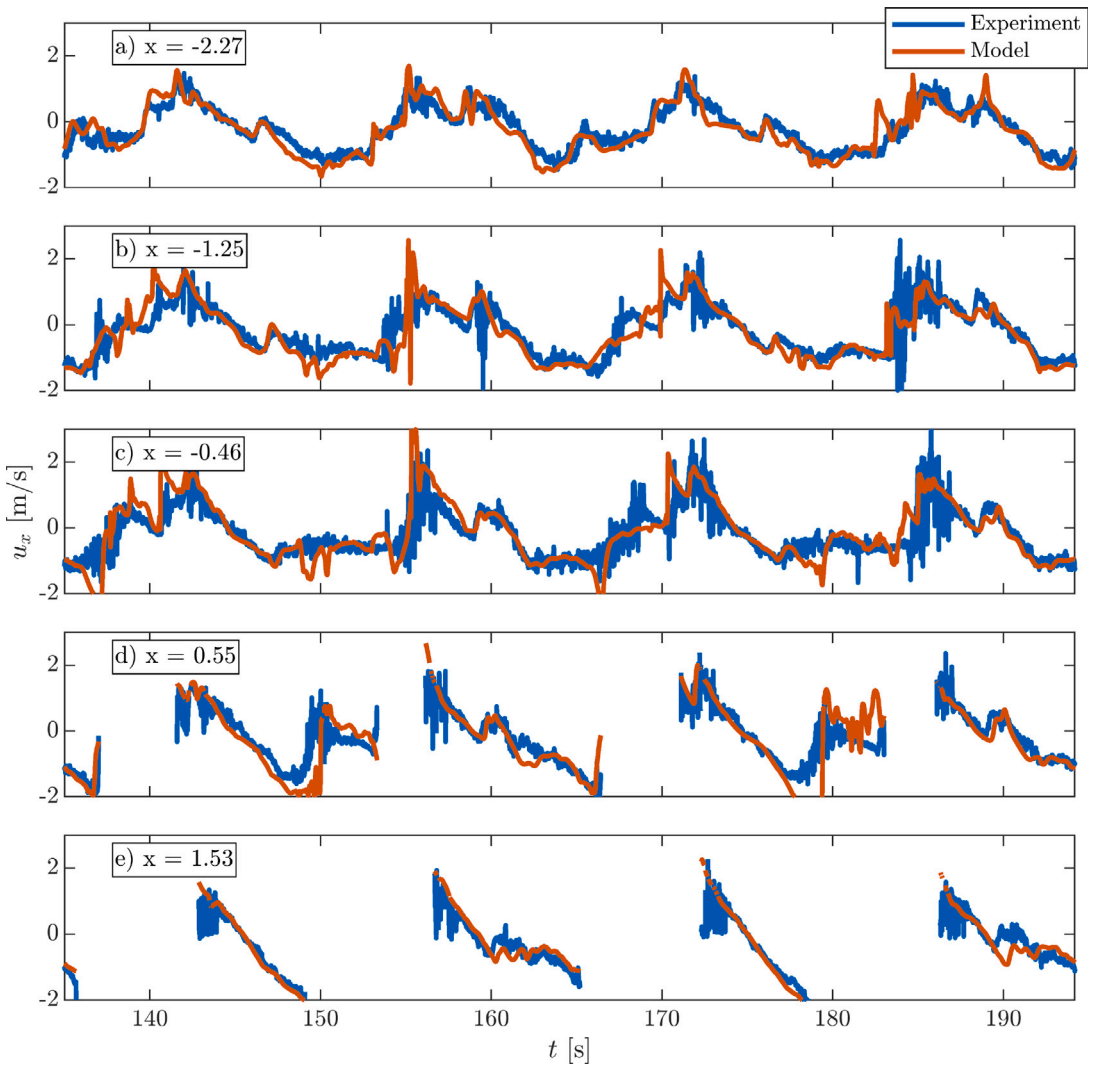

Fig. 9. Comparison between measured and modelled velocities at 3 cm above the bed at five different cross-shore locations, made using model configuration D. In panels (d) and (e) data is omitted when the ADV probe is exposed to air.

that vertical nonuniformities are indeed important for determining the suspended sediment flux in the swash zone.

5. Discussion

5.1. Dealing with bubbles

The results show that care needs to be taken when modelling the air/water interface close to the bed. For instance, the presence of numerical ventilation can lead to unphysical air bubbles sticking to the bed. Furthermore, a 2DV approach can mean that bubbles do not rise correctly. Previous research has shown that certain coastal processes are inherently 3D. For instance, there are large-scale 3D structures present around the process of wave-breaking (Dalrymple and Rogers, 2006; Tazaki et al., 2022). Furthermore, small-scale turbulence presents 3D characteristics. Complementing these, Appendix A shows that also bubble break-up and rise is a 3D process that needs to be carefully considered when one models the presence of bubbles in a 2D setting.

There are many different ways one can deal with this issue. One way is accepting that a 3D model is required for the problem. This is of course in many applications not feasible. In this thesis we chose to define restrictions on where bubbles are allowed, and remove them when they are deemed unphysical. This means bubbles are removed, but a penalty to the conservation of water mass is paid. Also, the choice of criteria is not immediately clear and can therefore lead to additional model uncertainty. This approach is similar to an approach taken in planing hull simulations (Viola et al., 2012; Mancini et al., 2016).

To quantify the effects of the added water, a comparison is made with the total volume of water in the domain between configurations A and B. Fig. 12 shows the evolution of the total volume in these configurations over time and the difference in volume between both configurations. The maximum difference is approximately 0.3 m^2, which amounts to less than half a percent of the total volume. This has the effect of locally raising the water levels in the swash (see Fig. B.14 in B). This can be explained by a combination of the added water mass to the domain and the increased friction in the swash for Configurations B and D locally increasing the water depth. Close to the paddle, the relaxation zone used to generate the waves keeps the average water level steady, meaning that the added water can leave the domain.

Another way of dealing with this is to remove the air phase from the VoF implementation. This is the approach used by García-Maribona et al. (2021, 2022), which also explains the lack of air under broken bores in their results. This was until recently not available in OpenFOAM, however, a novel study has implemented such a model in the OpenFOAM environment (Qwist and Christensen, 2023). In these methods, air is not conserved which could lead to different flow behaviour where air content is important, such as breaking waves and bores. The importance of modelling air conservation is, to the knowledge of

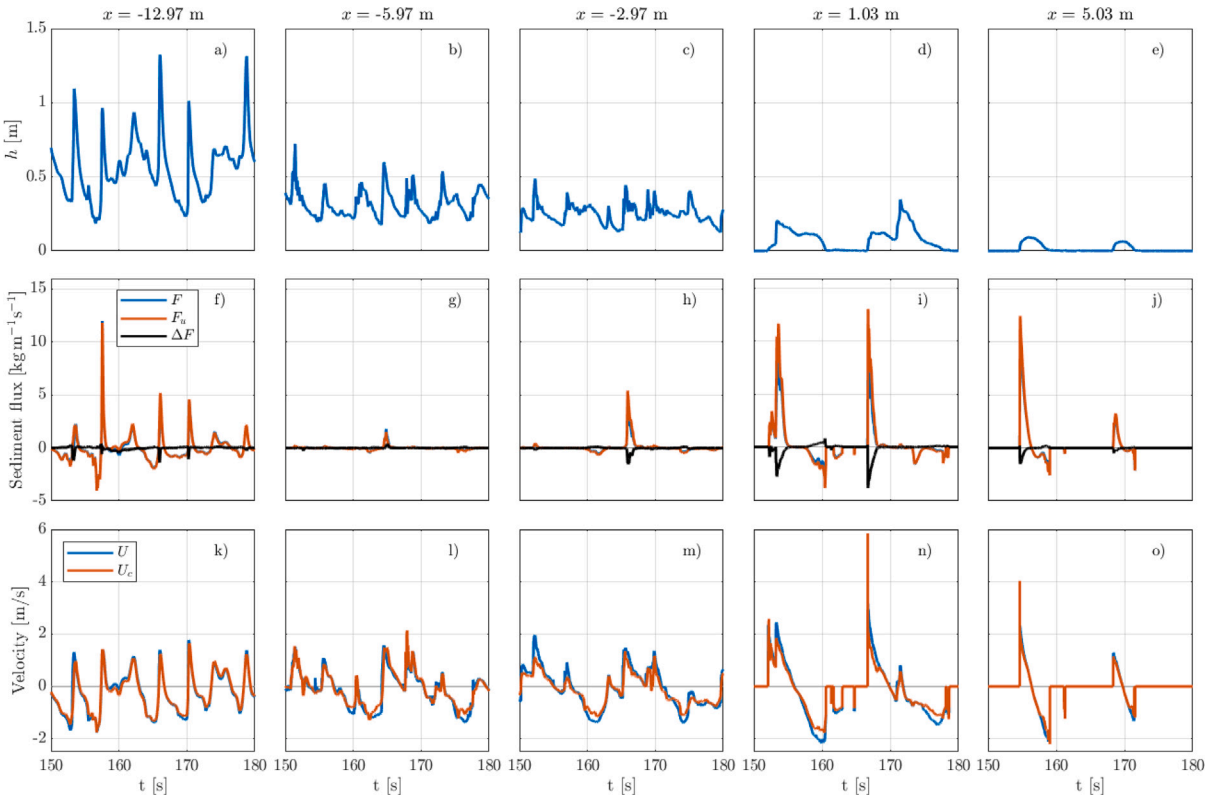

Fig. 10. Figure showing (a–e) water depth, (f–j) sediment fluxes and (k–o) transport velocities for five different cross-shore locations.

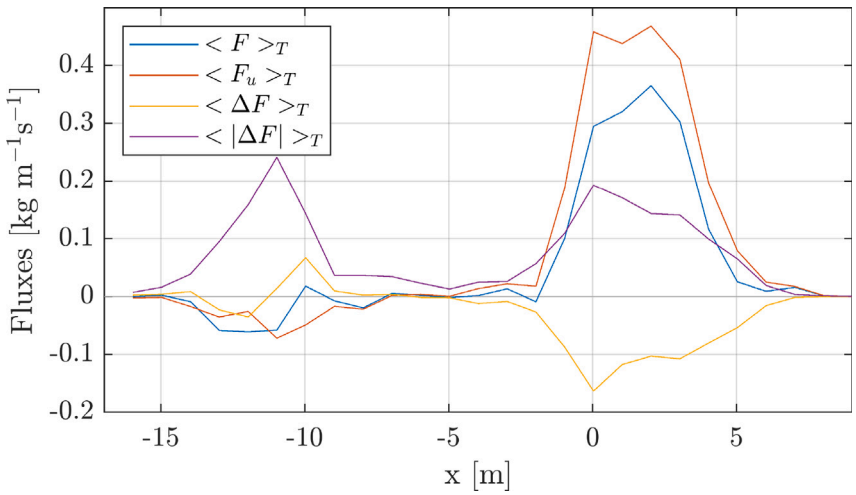

Fig. 11. Figure showing the time-averaged fluxes F, F_u and Δ_F. Here the interval $T = [135\,\mathrm{s}, 135 + 3T_r\,\mathrm{s}]$.

the authors, not yet understood, and is something that requires more investigation.

In our study we used the VoF method and specifically the isoAdvector implementation. There are also alternatives for determining the free surface, such as for instance the level set method. However, when this method is used, the bubbles disappear because these methods strictly do not conserve mass. Recent studies have introduced ways to correct this by coupling the level set method with the VoF method (Kim and Park, 2021; Xia and Kamlah, 2022). However, this means that, in effect, we are back to the situation with 2D bubbles, which we have shown show unphysical bubble rise behaviour. Alternatively, a different VoF method, such as the default MULES (Ubbink, 1997; Rusche, 2002) method can be used. This method produces smoother interfaces compared with isoAdvector and as such could pose a solution to the small bubbles. However, as detailed in Roenby et al. (2016), isoAdvector was designed precisely to generate sharp interfaces between fluids, which is physically more accurate.

Finally, one can model bubbles in a similar manner this study approaches suspended sediment, by viewing dispersed bubbles as a continuous field with a concentration, which is modelled according to a conservation law. This has previously been successfully done for breaking waves (e.g. Shi et al., 2010; Derakhti and Kirby, 2014; Castro et al., 2016), however to the authors' knowledge this has not yet been applied to simulations involving sediment transport or in the swash zone.

For modellers, the most important take-away from this discussion is that it matters how one deals with bubbles and the air/water interface. Depending on the application, some methods are more suitable than

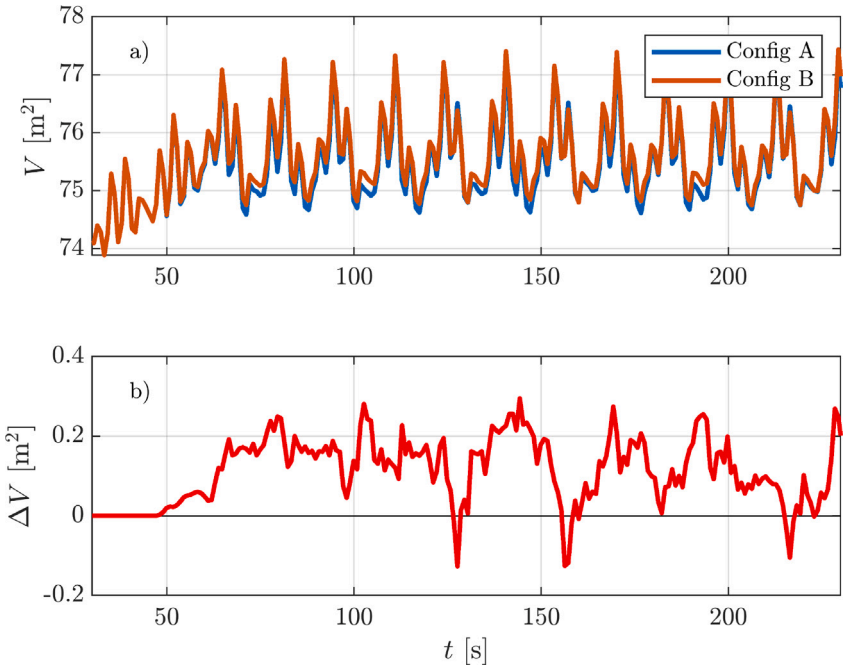

Fig. 12. Time series of the total volume of water in the domain for Configurations A and B (panel a) and the difference between these Configurations (panel b).

others. For instance, 3D simulations are in many situations not suitable. For coastal applications, it could be fruitful to study the importance of air-conservation under breaking waves and bores, as methods that do not require computations in the air phase are computationally more efficient. Furthermore, the method of modelling bubbles as a dispersed phase could be a promising, physics-based approach. Finally, the phenomenon of numerical ventilation needs to be better understood. This has, to the authors' knowledge not been studied in a coastal context. An analysis of these methods and their impact on sediment transport would be a valuable endeavour.

5.2. Turbulence

It is widely accepted that bore-related turbulence is an essential driver for sediment transport in the swash zone (e.g. Butt et al., 2004; Alsina et al., 2009; Zhu and Dodd, 2020). This is again affirmed in the present study, which shows that the limiter for the $k-\omega$ model, introduced by Wilcox (2006) in this situation leads to underpredicted sediment concentrations, and as such can be presumed to underpredict turbulent kinetic energies as well. This limiter was introduced to better capture flow separation phenomena in compressible flows in the presence of a shock (Coakley, 1983). This is a different application than water waves, which are usually modelled as incompressible and as such no shocks occur. Our results suggest that the limiter can lead to underpredicted sediment concentrations in the uprush. To definitively conclude this though, this should be investigated for more cases.

There are various studies on the suitability of RANS turbulence closures and modifications to them. For instance the study by Brown et al. (2016) analysed turbulence closures under plunging and spilling breakers. Furthermore, Devolder et al. (2018) analysed a buoyancy production modification specifically for free-surface waves and the aforementioned (Larsen and Fuhrman, 2018) limiter addresses the overproduction issue many two-equation RANS turbulence closures posses. Recently, a stress-ω model by Li et al. (2022) showed that their model both improved velocity profiles in the surf zone, and resulted in larger Reynolds shear stresses in the inner surf zone.

These are important and promising results for sediment transport. However, it is not always straightforward to investigate their impact in the swash zone. Even though the goal of the present paper was not to investigate turbulence models in depth, we tried applying different flavours of turbulence models such as the Launder and Sharma (1974) $k-\epsilon$ model as implemented in Larsen and Fuhrman (2018), but also the nonlinear $k-\epsilon$ model (Shih et al., 1996) which (Brown et al., 2016) ranked the best among their studies. However, these models led to unphysically large eddy viscosities and velocities, which ultimately led to unstable simulations. This makes the study of turbulence models in the swash zone, and their verification for sediment transport, very difficult to do.

5.3. Model performance

The comparison of the modelled hydrodynamics with the wave gauges and ADVs show that the model performs well. The performance is similar to the model study of Larsen et al. (2020), who also used a RANS and VoF model based on OpenFOAM for studying turbulence under plunging bichromatic waves, and the study of Losada et al. (2008) who used the COBRAS model. Both models show small discrepancies at the crest of the wave group envelope, and larger differences at the trough of the wave group envelope. A comparison with measurements of modelled flow velocities shows that the model performs well in this respect as well. The quality of the simulation is similar at all five locations. The largest differences happen around quick jumps in velocity. Previous studies conducting 3D simulations have shown that the flow is inherently 3D (e.g. Dalrymple and Rogers, 2006; Tazaki et al., 2022), which the 2DV model cannot capture, and could lead to some discrepancies.

The model predicts onshore-directed suspended sediment transport, whereas the experiments show mild accretion high in the swash. This can also be seen in Fig. 5, where model configuration *D* shows high sediment concentrations in the uprush but low sediment concentrations in the backwash, especially at the two most onshore locations. During uprush these concentrations correspond well with the measurements,

but later towards the backwash the model predicts significantly lower concentrations than the measurements. Because of this, one can assume that the model performs reasonably well in the uprush, but has more difficulty in the backwash. Given the observations of Alsina et al. (2009) and Zhu and Dodd (2020), this suggests that the model accurately captures the suspended transport due to wave-breaking related turbulence and sediment advection, which is more important in the uprush, but underestimates the shear-related transport in the backwash. However, the different results from the four different configurations show that this balance is delicate and can be difficult to achieve. Currently, Configurations B and D remove all bubbles that remain close to the bed, whereas in reality some bubbles will still be present there. This suggests that the bubble-removal in these configurations perhaps is too aggressive. However, all four configurations generally show underpredicted sediment concentrations between the end of the uprush and the end of the backwash. This means that for all configurations sediment is not kept or brought into suspension enough at these moments. It is difficult to directly attribute a reason for this because the effects of errors in hydrodynamics and errors in the sediment transport modelling alone need to be separated. A possible explanation could be a general underprediction of turbulent mixing, which fails to keep sediment in suspension long enough. However, it is important to note that this is a comparison with point measurements, and that OBS probes can be sensitive to other impurities in the water such as air bubbles.

Finally, we note that the model is run for a situation where the experiments are almost at their (pseudo)-equilibrium, or at the very least show little morphological development compared with the start of the measurements. Due to minor differences between the model and the experiments, such as the different shapes of the paddles, 3D flow effects around the point of wave-breaking and nonuniformities in the alongshore direction, the model could tend to a different equilibrium than the experimental conditions. Furthermore, although bedload contributes less to the overall morphodynamics for these sediment characteristics in this model (Kranenborg et al., 2022), including bedload transport and intraswash morphodynamics in this study could improve flux predictions. The influence of this is seen in the measurements of water depths, for instance panels (f,g) in Fig. 8, where the negative water depths show that the bed level has decreased.

5.4. Vertical structures

The fluxes presented in Fig. 7 show strong vertical dependence in the time-averaged water and sediment fluxes. This is similar to the time-averaged fluxes presented by García-Maribona et al. (2022), who observed different sediment fluxes near the bed compared with higher in the water column (see Figure 14 in their paper). This is also seen on top of, and offshore from the main breaker bar in panel (h) of Fig. 7. García-Maribona et al. (2022) further point out that because of this, one can expect depth-averaged models (called 1D models in their paper) to have difficulty predicting suspended sediment fluxes.

In Section 4 we analysed the uniformity of the depth-dependent sediment transport flux at various locations in the surf and swash zones. An unexpected result is that, according to our results, around the point of wave-breaking, the suspended sediment flux can be thought of as being vertically uniform without a big concession in terms of sediment flux. This is different in the swash, where even though the flows are shallow, taking nonuniformities into account is clearly needed. Given that comparatively little sediment is exchanged between the surf and the swash, this is likely a local effect in the swash zone, and thus not dependent on the advection of pre-suspended sediment from the surf zone to the swash zone. This suggests that it is very important for depth-averaged models to both take this turbulent mixing and the vertical structures into account.

The uniform flux as defined in Eq. (13) is an interesting approach for the inclusion of vertical nonuniformities in a depth-averaged model. However, there are important differences between this analysis and an actual implementation in a depth-averaged model. Most importantly, the velocity and sediment distributions on which the uniform flux calculation is performed are still depth dependent. For this reason, the evolution of the suspended sediment by a depth-averaged model might differ more than the comparison between fluxes here suggests. A direct comparison between the fully depth-dependent flux, and a depth-averaged sediment model where the hydrodynamic input is the same could improve these findings further, and point to improvements that can lead to better depth-averaged flux calculations that can be practically implemented in depth-averaged models. Furthermore, to implement the effective velocity approach, first a suitable parametrisation needs to be formulated.

6. Conclusion

A 2DV, depth-resolving model, based on the model by Kranenborg et al. (2022) and Jacobsen et al. (2014) was used to analyse the suspended sediment transport under field-scale bichromatic waves. The model was applied to the experiments of Van der Zanden et al. (2019a) and was validated using measured surface elevations, flow velocities and sediment concentrations. Here, the answers to the research questions presented in the introduction are given.

What is the effect of the air entrainment and bubbles in a 2DV VoF model and how does it influence sediment transport?

It was noticed that an unphysical layer of air can stay near the bed, leading to decreased friction during the uprush. Furthermore, we showed that in 2DV models bubbles stay too long near the bed. These effects lead to a bias in the sediment transport towards the backwash, as uprush sediment transport is inhibited and backwash transport is enhanced due to the decreased uprush friction leaving the swash with more potential energy. To investigate the origin of this issue, a comparison was made between a 2DV and 3DV model of the bubble dynamics of an inverted air/water layer, see Appendix A. The models showed that bubbles rise considerably faster in a 3D model compared with a 2DV model. When these parasitic bubbles were removed from the swash zone model, the increased friction during uprush and decreased friction during backwash lead to stronger onshore net transport fluxes, improving model predictions of suspended sediment concentrations.

What is the influence of the Wilcox (2006) limiter on wave-breaking turbulence and sediment transport?

A similarly important effect on sediment transport was noticed when the effect of the (Wilcox, 2006) limiter on sediment transport was analysed. When this limiter was deactivated, turbulence and in turn the eddy viscosity was increased from the region of wave-breaking and onshore. This led to increased sediment transport, especially during uprush.

The combination of both effects mentioned above was needed to achieve adequate sediment behaviour. In fact, these adaptations lead to significantly different sediment dynamics, as shown in Fig. 7. The same figure shows very small differences in mean flow velocities. This shows that the quality of modelled flow velocities and water depths alone are not a good enough for achieving correct sediment transport results, and that small differences in turbulence model and small quantities of parasitic bubbles near the bed can have large impacts on the quality of the sediment transport predictions.

How do vertical structures in sediment concentration and flow velocity influence the sediment transport flux?

The final validated model shows that the effect of nonuniformities in the cross-shore velocity and suspended sediment concentration have a large influence on the total sediment flux in the swash. More precisely, when uniform flow velocities and sediment concentrations were assumed, net sediment transport fluxes were overpredicted. To compensate for this, depth-averaged models would require a lower

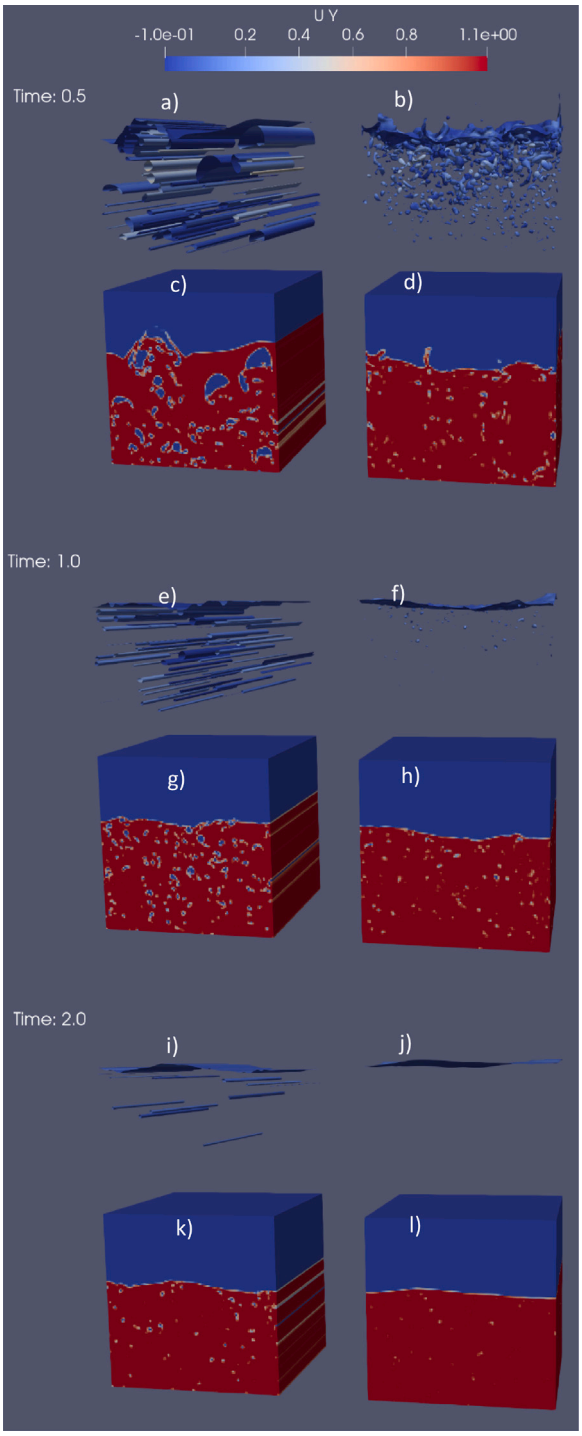

Fig. A.13. Figure showing three snapshots of the 2D and 3D models of bubbles escaping from an inverted air/water layer. Here panels (c, d, g, h, k, l) show the simulations of the α field from a side perspective. Above the blocks (panels a, b, e, f, i, j) are isosurfaces where $\alpha = 0.5$ are shown, where the colour indicates the vertical velocity in positive upward direction. The left column shows the 2D results and the right column shows the 3D results. Panels (a–d) show the situation at $t = 0.5$ s, panels (e–h) show the situation at $t = 1$ s and panels (i–l) show the situation at $t = 2$ s.

effective transport velocity compared with the depth-averaged velocity in the sediment transport calculations. These findings are in contrast with the region of intense wave-breaking where, although a large amount of sediment is being transported, these vertical nonuniformities are less important to take into account in the net flux calculations.

CRediT authorship contribution statement

J.W.M. Kranenborg: Writing – review & editing, Writing – original draft, Software, Methodology, Investigation, Formal analysis, Conceptualization. **G.H.P. Campmans:** Writing – review & editing, Supervision, Methodology, Conceptualization. **J.J. van der Werf:** Writing – review & editing, Supervision, Project administration, Methodology, Conceptualization. **R.T. McCall:** Writing – review & editing, Supervision, Conceptualization. **A.J.H.M. Reniers:** Writing – review & editing, Supervision, Methodology, Investigation, Funding acquisition, Formal analysis, Conceptualization. **S.J.M.H. Hulscher:** Writing – review & editing, Supervision, Project administration, Methodology, Funding acquisition, Conceptualization.

Declaration of competing interest

The authors declare that they have no known competing financial interests or personal relationships that could have appeared to influence the work reported in this paper.

Data availability

Data will be made available on request.

Acknowledgements

This work is part of the research program Shaping The Beach with project number 16130, which is financed by the Netherlands Organisation for Scientific Research (NWO), with in-kind support by Deltares. The model simulations were carried out on the Dutch national e-infrastructure with the support of SURF Cooperative. We thank Aline Valster from the Twente Writing Centre for her feedback on the manuscript. We also acknowledge the constructive criticism from an expert reviewer.

Appendix A. 3D vs 2D bubble effects

To better understand what happens to bubbles in the model, we set up a different model experiment solely focussed on bubble dynamics when a layer of air is present under a layer of water. We look at a cubic domain with sides $l = 0.1$ m. The initial condition is partitioned in three vertical layers. At the bottom there is a layer of air ($\alpha = 0$) with a thickness of $h_{air} = 0.01$ m. Next is a layer of water, with a thickness of $h_{water} = 0.07$ m. Finally, at the top there is a layer of air again.

The domain is discretised in a 2D and a 3D configuration. In both models, the x and y directions are discretised in 100 equidistant layers of cells. For the 3D case, also the z direction is discretised in 100 layers. This means that the 2D model consists of 10 000 cells, and the 3D model consists of 1000 000 cells. In this case the boundary conditions at the walls are slip conditions, and the atmosphere condition is the same as explained in Section 2.2.3. Finally at the bottom wall a no-slip condition is imposed. To keep these cases as simple as possible, no turbulence was modelled, meaning only the fluid viscosities contributed to the momentum diffusion.

Fig. A.13 shows the results, comparing the 2D and 3D cases. Qualitatively there is a big difference between the two solutions that is immediately visible. In the 3D case, bubbles look natural and as expected have a 3D shape to them. However, this is not possible in the 2D case, meaning that the bubbles in fact represent long cylinders, as there is only one cell in the z direction. This also means that, even though in panels (g) and (h) the solution looks similar on the boundary, the amount of air in the domain is very different, as seen in panels (e) and (f). Looking even later in the simulation at $t = 2$ s, there are still significant bubbles present in the 2D simulation, see panel (i), whereas panel (j) displays no more bubbles. Note that some air is still visible

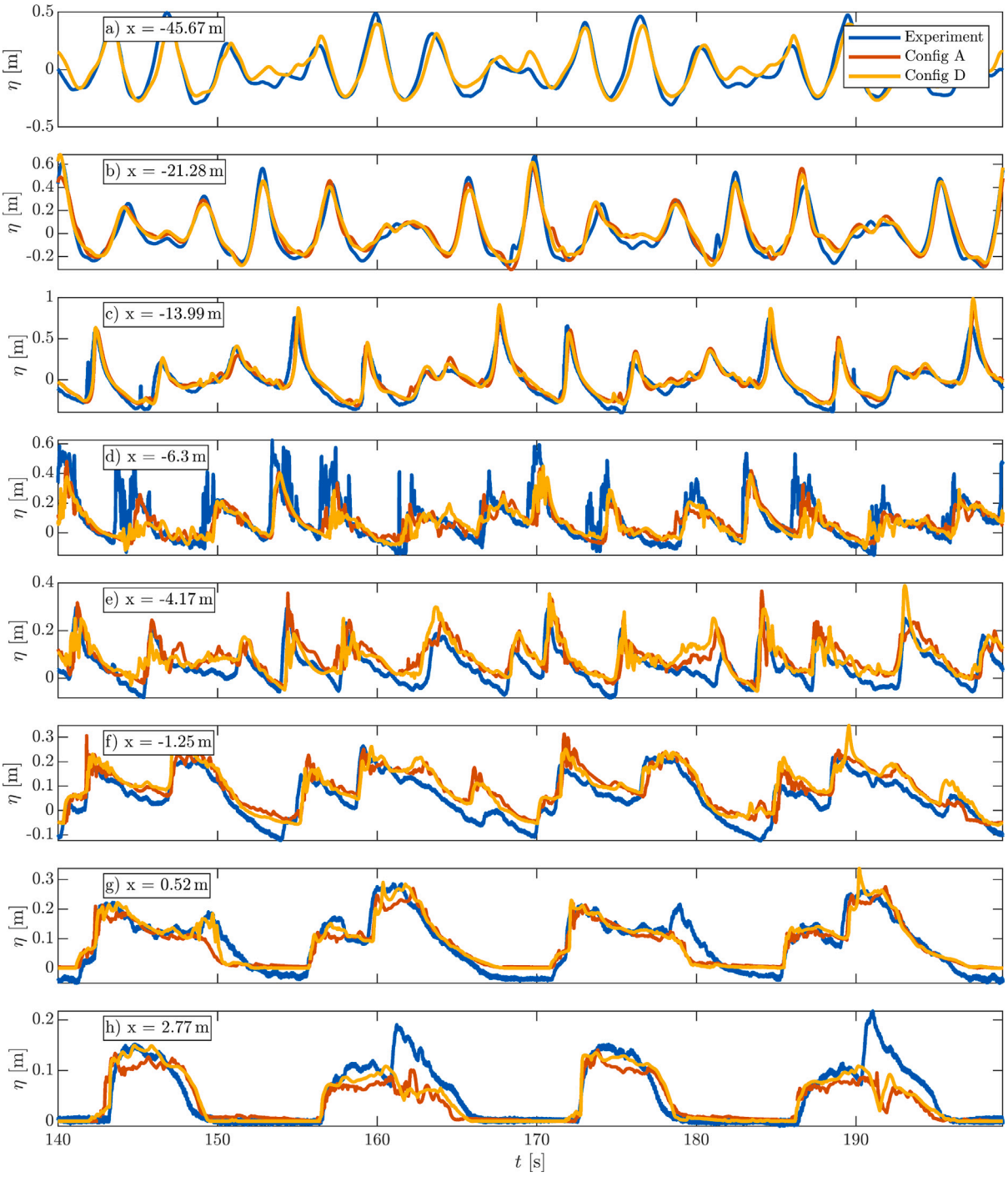

Fig. B.14. Comparison of water levels between measurements and model Configurations A and D.

in panel (*l*); this air is not visible in panel (*j*), this is solely due to the isosurface value of $\alpha = 0.5$.

The difference between the 2D and 3D bubbles simulations show that in a 2D simulation, bubbles take much more time to reach the surface. Moreover, bubbles also stay close to the bottom for longer than in the 3D simulation. The explanation for this comes from the fact that, for the 2D situation, water has only one degree of freedom in which it can flow around the bubble. In the 3D situation, bubbles are allowed to break up, and water is allowed to flow around bubbles in two degrees of freedom. This effectively means that the friction bubbles experience in the 2D situation is much larger than in the 3D situation.

Appendix B. Comparison between Configurations A and D

Figs. B.14 and B.15 show comparisons of wave gauges and flow velocities between model Configurations A and D. The water levels show little difference between the configurations. This is especially true the closer one gets to the paddle. At the beach end, Configuration D produces slightly larger water depths. The flow velocities similarly show little qualitative difference. The largest differences occur when either model produces a spiky signal, which indicates presence of a bore or a similar phenomenon where velocities fluctuate rapidly. The calmer signal between these events coincide well between both model Configurations.

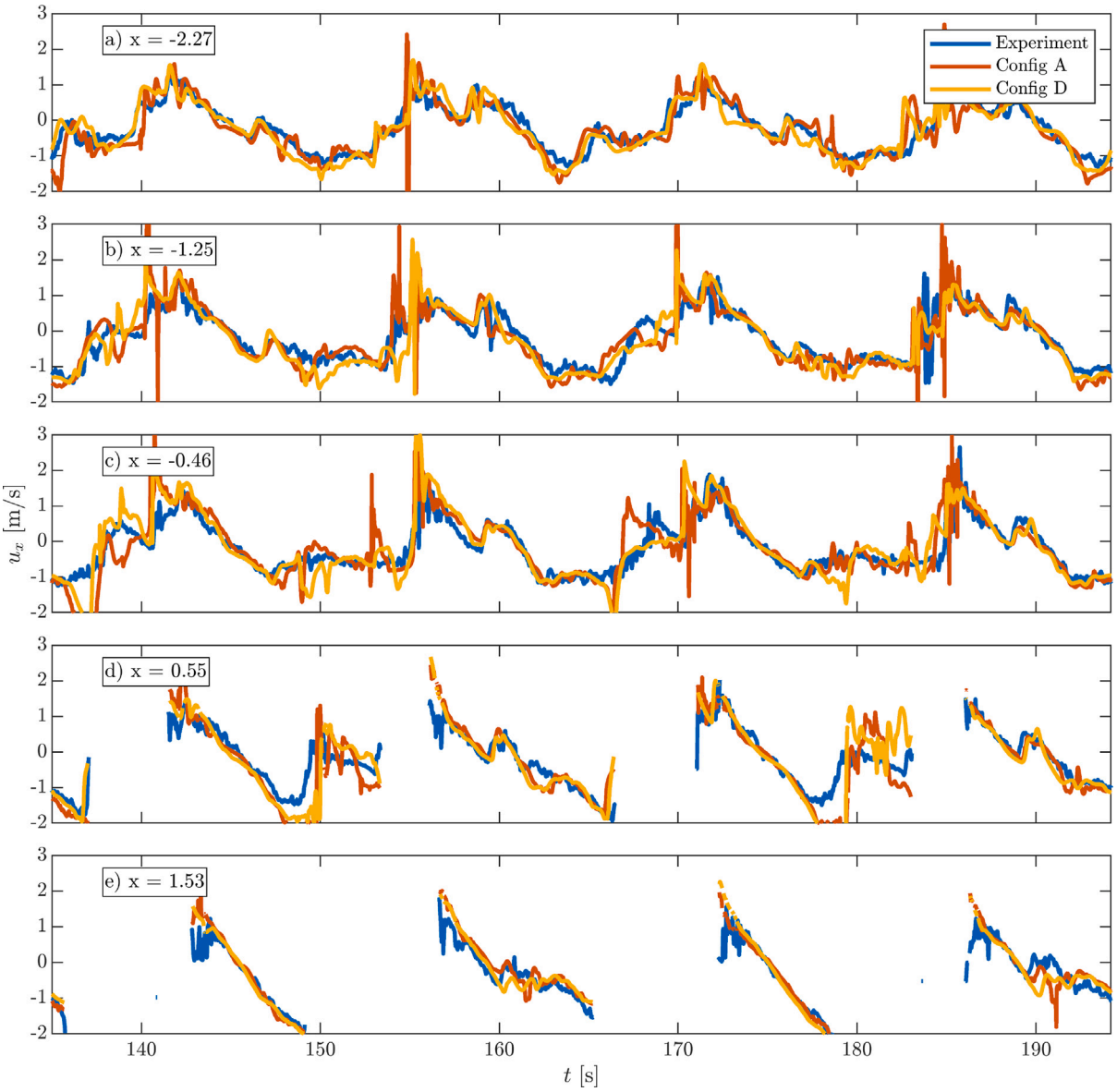

Fig. B.15. Comparison of velocities between measurements and model Configurations A and D.

References

Aagaard, T., Brinkkemper, J., Christensen, D.F., Hughes, M.G., Ruessink, G., 2021. Surf zone turbulence and suspended sediment dynamics— A review. J. Mar. Sci. Eng. 9 (11), 1300. http://dx.doi.org/10.3390/jmse9111300, Publisher: Multidisciplinary Digital Publishing Institute.

Alsina, J.M., Falchetti, S., Baldock, T.E., 2009. Measurements and modelling of the advection of suspended sediment in the swash zone by solitary waves. Coast. Eng. 56 (5–6), 621–631. http://dx.doi.org/10.1016/j.coastaleng.2009.01.007, Publisher: Elsevier B.V. ISBN: 0378-3839.

Blenkinsopp, C.E., Turner, I.L., Masselink, G., Russell, P.E., 2011. Swash zone sediment fluxes: Field observations. Coast. Eng. 58 (1), 28–44. http://dx.doi.org/10.1016/j.coastaleng.2010.08.002, Publisher: Elsevier B.V..

Briganti, R., Torres-Freyermuth, A., Baldock, T.E., Brocchini, M., Dodd, N., Hsu, T.J., Jiang, Z., Kim, Y., Pintado-Patiño, J.C., Postacchini, M., 2016. Advances in numerical modelling of swash zone dynamics. Coast. Eng. 115 (May), 26–41. http://dx.doi.org/10.1016/j.coastaleng.2016.05.001, ISBN: 0378-3839.

Brown, S.A., Greaves, D.M., Magar, V., Conley, D.C., 2016. Evaluation of turbulence closure models under spilling and plunging breakers in the surf zone. Coast. Eng. 114, 177–193. http://dx.doi.org/10.1016/j.coastaleng.2016.04.002, Publisher: Elsevier B.V..

Butt, T., Russell, P., Puleo, J., Miles, J., Masselink, G., 2004. The influence of bore turbulence on sediment transport in the swash and inner surf zones. Cont. Shelf Res. 24 (7–8), 757–771. http://dx.doi.org/10.1016/j.csr.2004.02.002.

Castro, A.M., Li, J., Carrica, P.M., 2016. A mechanistic model of bubble entrainment in turbulent free surface flows. Int. J. Multiph. Flow 86, 35–55. http://dx.doi.org/10.1016/j.ijmultiphaseflow.2016.07.005, Publisher: Pergamon.

Cebeci, T., Chang, K.C., 1978. Calculation of incompressible rough-wall boundary-layer flows. AIAA J. 16 (7), 740–746. http://dx.doi.org/10.2514/3.7571.

Chen, W., Warmink, J.J., Van Gent, M.R.A., Hulscher, S.J.M.H., 2022. Numerical investigation of the effects of roughness, a berm and oblique waves on wave overtopping processes at dikes. Appl. Ocean Res. 118, 102971. http://dx.doi.org/10.1016/j.apor.2021.102971, Publisher: Elsevier.

Christoffersen, G., 2019. Laboratory scale CFD simulation of wave breaking and sediment transport (Ph.D. thesis). DTU, Copenhagen.

Coakley, T.J., 1983. Turbulence modeling methods for the compressible Navier-Stokes equations. http://dx.doi.org/10.2514/6.1983-1693, Publisher: Am. Inst. Aeronaut. & Astronaut.

Dalrymple, R.A., Rogers, B.D., 2006. Numerical modeling of water waves with the SPH method. Coast. Eng. 53 (2–3), 141–147. http://dx.doi.org/10.1016/j.coastaleng.2005.10.004, Publisher: Elsevier.

Deigaard, R., Fredsøe, J., Hedegaard, I.B., 1986. Suspended sediment in the surf zone. J. Waterw. Port Coast. Ocean Eng. 112 (1), 115–128. http://dx.doi.org/10.1061/(asce)0733-950x(1986)112:1(115), Publisher: American Society of Civil Engineers.

Derakhti, M., Kirby, J.T., 2014. Bubble entrainment and liquid-bubble interaction under unsteady breaking waves. J. Fluid Mech. 761, 464–506. http://dx.doi.org/10.1017/jfm.2014.637, Publisher: Cambridge University Press.

Devolder, B., Troch, P., Rauwoens, P., 2018. Performance of a buoyancy-modified k-ω and k-ω SST turbulence model for simulating wave breaking under regular waves

using OpenFOAM®. Coast. Eng. 138 (August 2017), 49–65. http://dx.doi.org/10.1016/j.coastaleng.2018.04.011, Publisher: Elsevier.
Engsig-Karup, A.P., Bingham, H.B., Lindberg, O., 2009. An efficient flexible-order model for 3D nonlinear water waves. J. Comput. Phys. 228 (6), 2100–2118. http://dx.doi.org/10.1016/j.jcp.2008.11.028.
Fredsøe, J., Deigaard, R., 1992. Mechanics of Coastal Sediment Transport, vol. 3, World Scientific, http://dx.doi.org/10.1142/1546, Series Title: Advanced Series on Ocean Engineering Publication Title: Coastal Engineering Issue: 1-2 ISSN: 03783839.
Fuhrman, D.R., Dixen, M., Jacobsen, N.G., 2010. Physically-consistent wall boundary conditions for the k-turbulence model. J. Hydraul. Res. 48 (6), 793–800. http://dx.doi.org/10.1080/00221686.2010.531100, Publisher: Taylor & Francis.
Galappatti, G., Vreugdenhil, C.B., 1985. Un modèle de transport solide en suspension intégré sur la verticale. J. Hydraul. Res. 23 (4), 359–377. http://dx.doi.org/10.1080/00221688509499345, Publisher: Taylor & Francis ISBN: 0022168850.
García-Maribona, J., Lara, J.L., Maza, M., Losada, I.J., 2021. An efficient RANS numerical model for cross-shore beach processes under erosive conditions. Coast. Eng. 170, 103975. http://dx.doi.org/10.1016/j.coastaleng.2021.103975, Publisher: Elsevier.
García-Maribona, J., Lara, J.L., Maza, M., Losada, I.J., 2022. Analysis of the mechanics of breaker bar generation in cross-shore beach profiles based on numerical modelling. Coast. Eng. 177, 104172. http://dx.doi.org/10.1016/j.coastaleng.2022.104172, Publisher: Elsevier.
Gray-Stephens, A., Tezdogan, T., Day, S., 2019. Strategies to minimise numerical ventilation in CFD simulations of high-speed planing hulls. In: Volume 2: CFD and FSI. American Society of Mechanical Engineers, Glasgow, Scotland, UK, http://dx.doi.org/10.1115/OMAE2019-95784, V002T08A042.
Incelli, G., Dodd, N., Blenkinsopp, C.E., Zhu, F., Briganti, R., 2016. Morphodynamical modelling of field-scale swash events. Coast. Eng. 115, 42–57. http://dx.doi.org/10.1016/j.coastaleng.2015.09.006, Publisher: Elsevier B.V..
Jacobsen, N.G., 2011. A Full Hydro- and Morphodynamic Description of Breaker Bar Development (Ph.D. thesis). Technical University of Denmark, Publication Title: Ph.D. thesis ISBN: 978-87-90416-64-5.
Jacobsen, N.G., Fredsoe, J., 2014a. Cross-shore redistribution of nourished sand near a breaker bar. J. Waterw. Port Coast. Ocean Eng. 140 (2), 125–134. http://dx.doi.org/10.1061/(asce)ww.1943-5460.0000233.
Jacobsen, N.G., Fredsoe, J., 2014b. Formation and development of a breaker bar under regular waves. Part 2: Sediment transport and morphology. Coast. Eng. 88, 55–68. http://dx.doi.org/10.1016/j.coastaleng.2014.01.015, Publisher: Elsevier BV.
Jacobsen, N.G., Fredsoe, J., Jensen, J.H., 2014. Formation and development of a breaker bar under regular waves. Part 1: Model description and hydrodynamics. Coast. Eng. 88, 182–193. http://dx.doi.org/10.1016/j.coastaleng.2013.12.008, Publisher: Elsevier B.V..
Jacobsen, N.G., Fuhrman, D.R., Fredsøe, J., 2012. A wave generation toolbox for the open-source CFD library: OpenFoam®. Internat. J. Numer. Methods Fluids 70 (9), 1073–1088. http://dx.doi.org/10.1002/fld.2726, Publisher: John Wiley & Sons, Ltd.
Jacobsen, N.G., Van Gent, M.R.A., Capel, A., Borsboom, M., 2018. Numerical prediction of integrated wave loads on crest walls on top of rubble mound structures. Coast. Eng. 142 (October), 110–124. http://dx.doi.org/10.1016/j.coastaleng.2018.10.004, Publisher: Elsevier.
Kim, H., Park, S., 2021. Coupled level-set and volume of fluid (Clsvof) solver for air lubrication method of a flat plate. J. Mar. Sci. Eng. 9 (2), 1–18. http://dx.doi.org/10.3390/jmse9020231, Publisher: Multidisciplinary Digital Publishing Institute.
Kranenborg, J.W.M., Campmans, G.H.P., Jacobsen, N.G., Van der Werf, J.J., Reniers, A.J.H.M., Hulscher, S.J.H.M., 2022. Depth-resolved modelling of intra-swash morphodynamics induced by solitary waves. J. Mar. Sci. Eng. 10 (9), 1175. http://dx.doi.org/10.3390/jmse10091175, Publisher: Multidisciplinary Digital Publishing Institute.
Larsen, B.E., Fuhrman, D.R., 2018. On the over-production of turbulence beneath surface waves in Reynolds-averaged Navier-Stokes models. J. Fluid Mech. 853, 419–460. http://dx.doi.org/10.1017/jfm.2018.577, Publisher: Cambridge University Press.
Larsen, B.E., Fuhrman, D.R., Baykal, C., Sumer, B.M., 2017. Tsunami-induced scour around monopile foundations. Coast. Eng. 129 (August), 36–49. http://dx.doi.org/10.1016/j.coastaleng.2017.08.002, Publisher: Elsevier Ltd.
Larsen, B.E., Van der A, D.A., Van der Zanden, J., Ruessink, G., Fuhrman, D.R., 2020. Stabilized RANS simulation of surf zone kinematics and boundary layer processes beneath large-scale plunging waves over a breaker bar. Ocean Model. 155, 101705. http://dx.doi.org/10.1016/j.ocemod.2020.101705, arXiv: 2010.14855 Publisher: Elsevier Ltd.
Launder, B.E., Sharma, B.I., 1974. Application of the energy-dissipation model of turbulence to the calculation of flow near a spinning disc. Lett. Heat Mass Transfer 1 (2), 131–137. http://dx.doi.org/10.1016/0094-4548(74)90150-7, Publisher: Pergamon.
Li, Y., Larsen, B.E., Fuhrman, D.R., 2022. Reynolds stress turbulence modelling of surf zone breaking waves. J. Fluid Mech. 937, 7. http://dx.doi.org/10.1017/jfm.2022.92.
Li, J., Qi, M., Fuhrman, D.R., 2019. Numerical modeling of flow and morphology induced by a solitary wave on a sloping beach. Appl. Ocean Res. 82 (October 2018), 259–273. http://dx.doi.org/10.1016/j.apor.2018.11.007, Publisher: Elsevier.
Losada, I.J., Lara, J.L., Guanche, R., Gonzalez-Ondina, J.M., 2008. Numerical analysis of wave overtopping of rubble mound breakwaters. Coast. Eng. 55 (1), 47–62. http://dx.doi.org/10.1016/j.coastaleng.2007.06.003, Publisher: Elsevier.
Mancini, G., Briganti, R., McCall, R., Dodd, N., Zhu, F., 2021. Numerical modelling of intra-wave sediment transport on sandy beaches using a non-hydrostatic, wave-resolving model. Ocean Dyn. 71 (1), 1–20. http://dx.doi.org/10.1007/s10236-020-01416-x, Publisher: Ocean Dynamics.
Mancini, S., Pensa, C., De Luca, F., Miranda, S., 2016. An extended verification and validation study of CFD simulations for planing hulls. J. Ship Res. 60, 101–118. http://dx.doi.org/10.5957/JOSR.60.2.160010.
Masselink, G., Puleo, J.A., 2006. Swash-zone morphodynamics. Cont. Shelf Res. 26 (5), 661–680. http://dx.doi.org/10.1016/j.csr.2006.01.015, ISBN: 0278-4343.
Paulsen, B.T., Bredmose, H., Bingham, H.B., 2014. An efficient domain decomposition strategy for wave loads on surface piercing circular cylinders. Coast. Eng. 86, 57–76. http://dx.doi.org/10.1016/j.coastaleng.2014.01.006, Publisher: Elsevier.
Qwist, J.R.K., Christensen, E.D., 2023. Development and implementation of a direct surface description method for free surface flows in OpenFOAM. Coast. Eng. 179, 104227. http://dx.doi.org/10.1016/j.coastaleng.2022.104227, Publisher: Elsevier.
Reniers, A.J.H.M., Gallagher, E.L., MacMahan, J.H., Brown, J.A., Van Rooijen, A.A., Van Thiel De Vries, J.S.M., Van Prooijen, B.C., 2013. Observations and modeling of steep-beach grain-size variability. J. Geophys. Res.: Oceans 118 (2), 577–591. http://dx.doi.org/10.1029/2012JC008073.
Roenby, J., Bredmose, H., Jasak, H., 2016. A computational method for sharp interface advection. R. Soc. Open Sci. 3 (11), 160405. http://dx.doi.org/10.1098/rsos.160405, arXiv: 1601.05392.
Ruffini, G., Briganti, R., Alsina, J.M., Brocchini, M., Dodd, N., McCall, R., 2020. Numerical modeling of flow and bed evolution of bichromatic wave groups on an intermediate beach using nonhydrostatic xbeach. J. Waterw. Port Coast. Ocean Eng. 146 (1), 04019034. http://dx.doi.org/10.1061/(asce)ww.1943-5460.0000530.
Rusche, H., 2002. Computational Fluid Dynamics of Dispersed Two-Phase Flows at High Phase Fractions (Ph.D. thesis). vol. 1, (December), p. 335, Publisher: Imperial College London (University of London) ISBN: 9781605587196.
Shi, F., Kirby, J.T., Ma, G., 2010. Modeling quiescent phase transport of air bubbles induced by breaking waves. Ocean Model. 35 (1–2), 105–117. http://dx.doi.org/10.1016/j.ocemod.2010.07.002, Publisher: Elsevier.
Shih, T.H., Zhu, J., Lumley, J.L., 1996. Calculation of wall-bounded complex flows and free shear flows. Internat. J. Numer. Methods Fluids 23 (11), 1133–1144. http://dx.doi.org/10.1002/(SICI)1097-0363(19961215)23:11<1133::AID-FLD456>3.0.CO;2-A.
Soulsby, R., 1997. Dynamics of Marine Sands: A Manual for Practical Applications. Telford, Publication Title: Dynamics of marine sands: a manual for practical applications.
Sumer, B.M., Guner, H.A.A., Hansen, N.M., Fuhrman, D.R., Fredsøe, J., 2013. Laboratory observations of flow and sediment transport induced by plunging regular waves. J. Geophys. Res.: Oceans 118 (11), 6161–6182. http://dx.doi.org/10.1002/2013JC009324.
Tazaki, T., Harada, E., Gotoh, H., 2022. Numerical investigation of sediment transport mechanism under breaking waves by DEM-MPS coupling scheme. Coast. Eng. 175, 104146. http://dx.doi.org/10.1016/j.coastaleng.2022.104146, Publisher: Elsevier.
Ting, F.C.K., Kirby, J.T., 1994. Observation of undertow and turbulence in a laboratory surf zone. Coast. Eng. 24 (1–2), 51–80. http://dx.doi.org/10.1016/0378-3839(94)90026-4, Publisher: Elsevier.
Ubbink, O., 1997. Numerical Prediction of Two Fluid Systems with Sharp Interfaces (Ph.D. thesis). Imperial College of Science, Technology and Medicine, London, Issue: January 1997 ISBN: 9781605586397 ISSN: 00219991.
Van der A, D.A., Van der Zanden, J., O'Donoghue, T., Hurther, D., Cáceres, I., McLelland, S.J., Ribberink, J.S., 2017. Large-scale laboratory study of breaking wave hydrodynamics over a fixed bar. J. Geophys. Res.: Oceans 122 (4), 3287–3310. http://dx.doi.org/10.1002/2016JC012072, Publisher: John Wiley & Sons, Ltd ISBN: 10.1002/2016.
Van der Zanden, J., Cáceres, I., Eichentopf, S., Ribberink, J.S., Van der Werf, J.J., Alsina, J.M., 2019a. Sand transport processes and bed level changes induced by two alternating laboratory swash events. Coast. Eng. 152, 103519. http://dx.doi.org/10.1016/j.coastaleng.2019.103519, Publisher: Elsevier B.V..
Van der Zanden, J., Van der A, D.A., Thorne, P.D., O'Donoghue, T., Ribberink, J.S., 2019b. Sand suspension and fluxes by wave groups and equivalent monochromatic waves. Cont. Shelf Res. 179, 85–104. http://dx.doi.org/10.1016/j.csr.2019.04.005, Publisher: Pergamon.
Viola, I.M., Flay, R.G.J., Ponzini, R., 2012. CFD analysis of the hydrodynamic performance of two candidate America's cup AC33 hulls. Trans. R. Inst. Nav. Archit. Part B: Int. J. Small Craft Technol. 154 (1), B1–B12. http://dx.doi.org/10.3940/rina.ijsct.2012.b1.113, Publisher: Royal Institution of Naval Architects.
Wilcox, D.C., 2006. Turbulence Modeling for CFD, 3rd edition DWC Industries, Inc..
Wilcox, D.C., 2008. Formulation of the k-ω turbulence model revisited. AIAA J. 46 (11), 2823–2838. http://dx.doi.org/10.2514/1.36541.
Xia, H., Kamlah, M., 2022. Modelling droplet evaporation with an improved coupled level set and volume of fluid (i-clsvof) framework. Proc. World Congress Mech., Chemi., Mater. Eng. http://dx.doi.org/10.11159/htff22.127, arXiv:2202.01019, ISBN: 9781990800108.
Zhu, F., Dodd, N., 2020. Swash zone morphodynamic modelling including sediment entrained by bore-generated turbulence. Adv. Water Resour. 146, 103756. http://dx.doi.org/10.1016/j.advwatres.2020.103756, Publisher: Elsevier Ltd.
Zyserman, J.A., Fredsøe, J., 1994. Data analysis of bed concentration of suspended sediment. J. Hydraul. Eng. 120 (9), 1021–1042. http://dx.doi.org/10.1061/(asce)0733-9429(1994)120:9(1021), Publisher: American Society of Civil Engineers.